

THESIS

THE EFFECTS OF TEMPERATURE-ELEVATION GRADIENTS ON SNOWMELT IN A HIGH-  
ELEVATION WATERSHED

Submitted by

Megan G. Sears

Department of Ecosystem Science and Sustainability

In partial fulfillment of the requirements

For the Degree of Master of Science

Colorado State University

Fort Collins, Colorado

Spring 2022

Master's Committee

Advisor: Steven Fassnacht

Stephanie Kampf  
Kristen Rasmussen

Copyright by Megan Grace Sears 2022

All Rights Reserved

## ABSTRACT

### THE EFFECTS OF TEMPERATURE-ELEVATION GRADIENTS ON SNOWMELT IN A HIGH-ELEVATION WATERSHED

The majority of snowmelt in the western U.S. occurs at high elevation where hydrometeorological measurements needed for monitoring snowpack processes are often in complex terrain. Data are often extrapolated based on point measurements at lower elevation stations and the elevation to be modeled. In this study, we compute near-surface air temperature-elevation gradients and dew point temperature-elevation gradients (TEG and DTEG, respectively) and compare values to widely accepted rates (e.g., environmental lapse rate). Further, the implications on snowmelt modeling of TEG and DTEG versus accepted temperature-elevation gradients are quantified using two index snowmelt models, 1) temperature and 2) temperature and radiation. TEG and DTEG were found to be highly variable and during nighttime often influenced by cold air drainage. Several modeling scenarios were applied that manipulated air temperature and dew point temperature, via incoming longwave radiation. When compared to the control scenario, these scenarios ranged in snow-all-gone date by -1 to +6 days. The model utilizing observed air temperature and an estimated DTEG performed most similarly to the control scenario. Thus, the estimated DTEG is adequate for index snowmelt models used in similar domains; however, further investigation should be done prior to applying the environmental lapse rate or other estimated TEG values.

## ACKNOWLEDGEMENTS

This research would not have been possible without the support of the Colorado Water Center. With their support I was able to purchase and deploy sensors in the study area. Second, I would like to thank my committee for all their continued guidance. Thank you to the several people who helped collect field data. I would also like to thank my husband, Tyler, who assisted with some of the field work and provided endless support. Finally, thank you to my family who has cheered me on through all my endeavors.

## TABLE OF CONTENTS

ABSTRACT.....	ii
ACKNOWLEDGEMENTS.....	iii
CHAPTER 1. INTRODUCTION.....	1
1.1 Background.....	1
1.2 Previous Work.....	5
1.3 Research Motivation.....	7
1.4 References.....	8
CHAPTER 2. RESEARCH INVESTIGATION.....	14
2.1 Introduction.....	14
2.2 Study Area and Datasets.....	18
2.2.1 Joe Wright Creek Study Area.....	18
2.2.2 Field Datasets.....	19
2.2.3 Spatial Datasets.....	20
2.3 Methodology.....	23
2.3.1 Temperature and dew point temperature elevation gradients.....	23
2.3.2 Observed SWE and snowmelt.....	25
2.3.3 Snowmelt modeling.....	25
2.4 Results.....	29
2.4.1 Observed air temperature and TEG.....	29
2.4.2 Observed dew point temperature and DTEG.....	36
2.4.3 Snowmelt modeling.....	41
2.5 Discussion.....	44
2.5.1 Observed air temperature and TEG.....	44
2.5.2 Observed dew point temperature and DTEG.....	46
2.5.3 Snowmelt modeling.....	47
2.6 Conclusions.....	49
2.7 References.....	50
CHAPTER 3. IMPLICATIONS AND FUTURE WORK.....	56

3.1	References .....	57
	APPENDIX A: SITE MAPS AND FIELD DATA LOCATIONS.....	58
	APPENDIX B: RESULTS.....	62

## CHAPTER 1. INTRODUCTION

### 1.1 Background

Accurately estimating water availability in a snowpack is critical for water managers since the western US water supply depends on snow accumulation and ablation (Pagano et al., 2004). Primary drivers for the accumulation of snow are cold air temperature for precipitation to fall as snow and persistence of colder than freezing temperatures to maintain the snowpack (Sospedra-Alfonso et al., 2015). Conversely, snowmelt is primarily driven by incoming shortwave and longwave radiation in mid-latitudes (Sicart et al., 2006). The spatial distribution of snow water equivalent or SWE (liquid water in a snowpack) has a substantial impact on snowmelt runoff magnitude in the Western US, making estimates of SWE key in forecasting water supply (Sexstone & Fassnacht, 2014). For much of the western US, water supply forecasts are made through regressions between historical runoff volumes, SWE measured at SNOTEL stations and snow courses (Church, 1933; Pagano et al., 2004; Schneider & Molotch, 2016). However, an issue in snow hydrology is that data are collected at different scales than are needed for forecasting (Blöschl, 1999). In the mountains, the majority of snowmelt occurs at high elevation where there are few hydrometeorological measurements to fully understand snowpack processes (Rolland, 2003). In addition to understanding the spatial variability of snow, melt rates and timing are required to accurately estimate snowmelt runoff characteristics, including the onset of melt and peak melt. Often these are estimated using snowmelt models (e.g., Follum et al., 2015, 2019; Hock, 1999; Kampf & Richer, 2014; Webb et al., 2017; Zhang et al., 2015).

Generally, snowmelt models fall into two categories: physically-based energy balance models, and empirical temperature index models (Hock, 2003). Often snowmelt modeling uses

the temperature index method due to its satisfactory performance and the wide availability of air temperature data, despite its computational simplicity (Hock, 2003). Such models are valuable to simulate snowmelt since temperature and precipitation are the only forcing variables (Follum et al., 2015). These models are based on an assumed relation between snowmelt and air temperature:

$$M=MF_i(T_a-T_{oi}) \quad (\text{Equation 1-1}),$$

where M represents the melt water per unit time,  $MF_i$  is a melt factor in melt degree per unit time,  $T_a$  is the air temperature over a specific time, and  $T_{oi}$  is the temperature at which melting is initiated. The melt factor, often considered as a function of time (Fassnacht et al., 2017), generally increases as solar radiation and elevation increase while sensible heat flux and albedo decrease (Hock, 2003). In temperature index models, air temperature is used as an index of the energy exchange between the snow surface and air (Anderson, 2006). However, air temperature is most directly correlated with longwave radiation (Ohmura, 2001), which represents only one component of the radiation budget. Additionally, temperature index models generally do not account for slope and aspect (Follum et al., 2015).

Studies have added radiation components to temperature index models to account for energy processes (Brubaker et al., 1996; Cazorzi & Dalla Fontana, 1996; Dunn & Colohan, 1999; Follum et al., 2015; Hamlin et al., 1998; Hock, 1999; Rango & Martinec, 1996). Hamlin (1998) sums Equation 1-1 with net radiation multiplied by a radiation melt factor ( $MF_{Hi}$ ):

$$M=MF_{Ti}(T_a-T_{oi})+MF_{Hi}(H_K^*+H_L^*) \quad (\text{Equation 1-2}),$$

where  $H_K^*$  is the net shortwave radiation and  $H_L^*$  is the net longwave radiation. When net radiation is added, the melt factor for air temperature becomes solely based on a temperature

melt factor (Hamlin et al., 1998). The added radiation components in the temperature index model yield more accurate snowmelt outputs (Follum et al., 2015, 2019; Hamlin et al., 1998; Kustas et al., 1994). In a case study of a small watershed in southern Colorado, the temperature index model with radiation provided better snow cover area estimates than the temperature index model in 75% of Landsat5 images (Follum et al., 2015). Additionally, another study found that the temperature index model with radiation generally improved the snowmelt estimates when compared to the index model using solely air temperature. Moreover, runoff was generated using snowmelt computations from both models and the temperature index model with radiation produced better results when compared to lysimeter data (Kustas et al., 1994).

Due to a lack of spatial measurements in a basin, near-surface air temperature, an essential meteorological variable in hydrologic modeling and critical in understanding mountain processes, is often extrapolated based on point measurements and elevation (Blandford et al., 2008; Collados-Lara et al., 2021; Harlow et al., 2004; Immerzeel et al., 2014; Lundquist & Cayan, 2007; Lute & Abatzoglou, 2020; Navarro-Serrano et al., 2018; Rolland, 2003; Shen et al., 2016). Such extrapolated near-surface air temperatures are commonly applied in hydrologic models (Garcia et al., 2013; Immerzeel et al., 2014; Kampf & Richer, 2014; Kulshrestha et al., 2018; Minder et al., 2010; Misra et al., 2020; Wang et al., 2016; Zhang et al., 2015). Generally, the change of temperature with elevation in the free atmosphere, the environmental lapse rate (ELR), averages about  $-6.5\text{ }^{\circ}\text{C}/\text{km}$  (Barry & Chorley, 1987). In practice, the change in near-surface air temperature-elevation gradient (TEG) is assumed to equal the environmental lapse rate. As indicated by the negative sign of the ELR, temperature typically decrease with increasing elevation. However, in some domains there can be increases of temperature with increased elevation, due to cold air drainage or pooling (Collados-Lara et al., 2021; Navarro-

Serrano et al., 2018). Cold air pooling is a stagnant layer of air that is colder than the air above it and often are diurnal and form during the evening or night and decay in the early morning. The cold air drainage or pooling are common features of mountainous topography (Whiteman et al., 2001). Additionally, the TEG varies temporally (seasonally and diurnally) and geographically (Blandford et al., 2008; Collados-Lara et al., 2021; Lundquist & Cayan, 2007; Lute & Abatzoglou, 2020; Navarro-Serrano et al., 2018; Rolland, 2003; Shen et al., 2016). Although there is a general understanding of TEG and the governing processes (e.g., radiative processes and atmospheric dynamics), estimating and applying to hydrologic modeling remains difficult.

Dew point temperature or relative humidity (RH) is critical when modeling energy and water balances, since it represents atmospheric moisture. The temperature at which the air will be saturated is the dew point temperature, i.e., when the air temperature equals the dew point temperature, the air is saturated (Feld et al., 2013). Incoming longwave radiation and latent heat flux are influenced by dew point temperature (Ruckstuhl et al., 2007). Air temperature and water vapor are often used to estimate incoming longwave radiation (Flerchinger et al., 2009). Greater dew point temperatures increase incoming longwave radiation since water vapor increases the atmospheric emissivity. When there is a small difference between air temperature and dew point temperature (i.e., vapor pressure deficit), there is less evaporation or sublimation occurring, which results in less latent heat exchange, i.e., less surface cooling (Feld et al., 2013). Despite the importance, atmospheric moisture, often represented as dew point temperature, is sparsely measured at high elevations with complex terrain. Similar to TEG, often only one point measurement is available and dew point temperatures are extrapolated from that measurement (Kunkel, 1989). Additionally, dew point temperature generally shows a decrease with elevation

(Feld et al., 2013). Other dew point temperature estimation methods include assuming it is equal to minimum daily temperature (Running and Ramakrishna, 1987).

## 1.2 Previous Work

Since air temperature is a required forcing variable in snowpack and hydrological models, determining an accurate TEG is essential. Several studies across different regimes have assessed the most accurate way to estimate TEG and compared the observed value to the ELR (Blandford et al., 2008; Collados-Lara et al., 2021; Immerzeel et al., 2014; Lundquist & Cayan, 2007; Minder et al., 2010; Shen et al., 2016). Harlow et al. (2004) indicated the ELR was applicable to a study area in south-eastern Arizona, but this region does not have topographic effects seen in TEG in mountainous regions where the ELR may not be suitable (Blandford et al., 2008; Collados-Lara et al., 2021; Lundquist & Cayan, 2007; Minder et al., 2010). Over a 10,000 km<sup>2</sup> area in south-central Idaho, the ELR grossly overestimated minimum and average temperatures and a monthly TEG, computed from synoptic weather type, was the most accurate (Blandford et al., 2008). Several other studies report that the TEG value should be used seasonally (summer TEG are greatest) or monthly, rather than annually (Immerzeel et al., 2014; Kulshrestha et al., 2018; Navarro-Serrano et al., 2018). Lute & Abatzoglou (2020) have found that using less than 5 temperature sensors can produce TEG error of several degrees Celsius per kilometer (°C/km). Observed TEG have been computed for various sized domains ranging from the hillslope scale (Collados-Lara et al., 2021) to the country of Spain (Navarro-Serrano et al., 2018). Collados-Lara et al. (2021) compared TEG of different spatial scales and reported that micro-scale analyses is necessary for validation of climatic products in mountains regions since the coarse-scale TEG did not show inversions or follow the ELR.

Multiple studies have focused on the impacts of changing the TEG values and the importance it has to the sensitivity and accuracy in the model (Garcia et al., 2013; Gardner & Sharp, 2009; Immerzeel et al., 2014; Kampf & Richer, 2014; Li & Williams, 2008; Martinec & Rango, 1986; Minder et al., 2010; Richard & Gratton, 2001; Tercek et al., 2021; Wang et al., 2016; Zhang et al., 2015), such studies have ranged in basin size from 64 km<sup>2</sup> to over 100,000 km<sup>2</sup> (Garcia et al., 2013; Wang et al., 2016). The TEG used in various models have been estimated using observed temperatures based on linear regression (Garcia et al., 2013; Immerzeel et al., 2014; Kampf & Richer, 2014; Minder et al., 2010; Richard & Gratton, 2001; Zhang et al., 2015), PRISM datasets (Garcia et al., 2013; Minder et al., 2010), Theissen weighted polygons of observed temperatures (Richard & Gratton, 2001), predetermined TEG using monthly variations for the Northern Hemisphere (Liston & Elder, 2006), and operational high resolution numerical weather prediction model simulations (Minder et al., 2010). A study in the Oregon Cascade Range indicated the snowmelt was most delayed when the ELR was used compared to weather stations and temperature modeled from the PRISM dataset (Garcia et al., 2013). Minder et al. (2010) found that using 200 m elevation zones in the Washington Cascades, the snowmelt shifted a full month earlier when the TEG was changed from -6.5 °C/km to -4.0 °C/km. Additional studies have shown that the sensitivity to the TEG used can show a 15 to 62% difference in simulated discharge (Wang et al., 2016; Zhang et al., 2015).

Similar to TEG, dew point temperature-elevation gradients (DTEG) are a rate of change in dew point temperature with elevation. Studies have estimated the DTEG using extrapolation from a point measurement, PRISM, an empirical relationship between air temperature and dew point temperature, mesoscale atmospheric models, a constant RH across a basin, and free-air observations (Cramer, 1961; Franklin, 1983; Kimball et al., 1997; Kunkel, 1989; Running &

Ramakrishna, 1987; Wigmosta et al., 1994). DTEG values determined from extrapolation of a point measurement have ranged from -1.25 (Cramer, 1961; Franklin, 1983) to -5.8 °C/km (Kunkel, 1989). Kunkel (1989) use monthly DTEG by varying the vapor pressure coefficient, which are estimates from radiosonde data for several stations averaged by month. Franklin (1989) and Cramer (1961) assume a constant DTEG. Running et al. (1983) assume dew point temperature to be equal to the minimum daily air temperature. Whereas, Kimball et al. (1997) incorporates the minimum and maximum daily air temperature, and the ratio of PET to annual precipitation. Feld et al. (2013) includes all of the above dew point temperature methods and compares the values with elevation changes to observed. It was found that the WRF model produced the best results when compared to observed values (Feld et al., 2013).

While several studies have examined techniques to estimate DTEG, few studies have applied these techniques to quantify the hydrological impacts. Feld et al. (2013) utilized temperature (applying the ELR) and RH (assumed constant) to determine the dew point temperature. To understand the implications of using different dew point temperature estimations, Feld et al. (2013) added scenarios of  $\pm 2$  °C to the base dew point temperature over a 7-year period. With these scenarios, Feld et al. (2013) found an average of  $\pm 2$  W/m<sup>2</sup> incoming longwave radiation and  $\pm 3$  days in snow-all-gone. Notably, dew point temperature estimation errors increased during the summer when evapotranspiration (ET) was at its largest. Therefore, properly estimating dew point temperature or DTEG is essential for basins where ET is an important driver (Feld et al., 2013).

### **1.3 Research Motivation**

There have been studies located within the Cache la Poudre basin that have focused on TEG (Collados-Lara et al., 2021; Kampf & Richer, 2014). While Collados-Lara et al. (2021)

focused on fine-scale temperature measurements (i.e., 50-m spacing, the data were not applied to modeling due to the limited temporally extent. DTEG has not been studied in Cache la Poudre basin. Using techniques and background information from previous local studies, we focused on a finer spatial scale (i.e., sensors located every 50 m of elevation increase) and the impacts of TEG and DTEG on snowmelt modeling over an 8.8 km<sup>2</sup> watershed. Further, this study is located nearby the Cameron Peak Fire, which burned over 200,000 acres and is the largest fire in Colorado history (< <https://source.colostate.edu/csu-team-lands-nsf-award-to-study-streams-snowpack-in-cameron-peak-fire-area/>>, accessed September 5, 2021). Understanding TEG and DTEG in subalpine to alpine environments within the Cache la Poudre can contribute to the extensive research that is being completed to understand wildfire impacts, specifically in persistent snow zones.

Since snowmelt, ecological, and hydrological modeling efforts use TEG and DTEG to estimate forcing data (temperature and RH) from station data across an area with variation in elevation, this study evaluates the significance of TEG and DTEG for a small snow-dominated watershed that is located within alpine and subalpine environments. This research examines the impact of using observed TEG and DTEG versus published values to model snowmelt at high elevation watershed. Furthermore, as the climate changes, understanding TEG and its importance to snowmelt timing is essential for water resource managers. This study provides insight to researchers and managers on whether utilizing the published TEG or DTEG is appropriate for estimating runoff in headwater environments.

#### **1.4 References**

Anderson, E. (2006). *Snow Accumulation and Ablation Model–SNOW-17*. U.S. National Weather Service.  
<https://www.wcc.nrcs.usda.gov/ftpref/wntsc/H&H/snow/AndersonSnow17.pdf>

- Barry, R., & Chorley, R. (1987). *Atmosphere, Weather, and Climate* (1<sup>st</sup> ed.). Associated Book Publishers.
- Blandford, T. R., Humes, K. S., Harshburger, B. J., Moore, B. C., Walden, V. P., & Ye, H. (2008). Seasonal and synoptic variations in near-surface air temperature lapse rates in a mountainous basin. *Journal of Applied Meteorology and Climatology*, *47*(1), 249–261. <https://doi.org/10.1175/2007JAMC1565.1>
- Blöschl, G. (1999). Scaling issues in snow hydrology. *Hydrological Processes*, *13*(14–15), 2149–2175. [https://doi.org/10.1002/\(SICI\)1099-1085\(199910\)13:14/15<2149::AID-HYP847>3.0.CO;2-8](https://doi.org/10.1002/(SICI)1099-1085(199910)13:14/15<2149::AID-HYP847>3.0.CO;2-8)
- Brubaker, K., Rango, A., & Kustas, W. (1996). Incorporating radiation inputs into the snowmelt runoff model. *Hydrological Processes*, *10*(10), 1329–1343. [https://doi.org/10.1002/\(sici\)1099-1085\(199610\)10:10<1329::aid-hyp464>3.0.co;2-w](https://doi.org/10.1002/(sici)1099-1085(199610)10:10<1329::aid-hyp464>3.0.co;2-w)
- Cazorzi, F., & Dalla Fontana, G. (1996). Snowmelt modelling by combining air temperature and a distributed radiation index. *Journal of Hydrology*, *181*(1–4), 169–187. [https://doi.org/10.1016/0022-1694\(95\)02913-3](https://doi.org/10.1016/0022-1694(95)02913-3)
- Church, J. E. (1933). Snow Surveying: Its Principles and Possibilities. *Geographical Review*, *23*(4), 529. <https://doi.org/10.2307/209242>
- Collados-Lara, A. J., Fassnacht, S. R., Pulido-Velazquez, D., Pfohl, A. K. D., Morán-Tejeda, E., Venable, N. B. H., Pardo-Igúzquiza, E., & Puntenney-Desmond, K. (2021a). Intra-day variability of temperature and its near-surface gradient with elevation over mountainous terrain: Comparing MODIS land surface temperature data with coarse and fine scale near-surface measurements. *International Journal of Climatology*, *41*, E1435–E1449. <https://doi.org/10.1002/joc.6778>
- Cramer, O. (1961). Adjustment of relative humidity and temperature for differences in elevation. *USDA Forest Service, Pacific Northwest Research Station*, 1–21.
- Dunn, S. M., & Colohan, R. J. E. (1999). Developing the snow component of a distributed hydrological model: A step-wise approach based on multi-objective analysis. *Journal of Hydrology*, *223*(1–2), 1–16. [https://doi.org/10.1016/S0022-1694\(99\)00095-5](https://doi.org/10.1016/S0022-1694(99)00095-5)
- Fassnacht, S. R., López-Moreno, J. I., Ma, C., Weber, A. N., Pfohl, A. K. D., Kampf, S. K., & Kappas, M. (2017). Spatio-temporal snowmelt variability across the headwaters of the Southern Rocky Mountains. *Frontiers in Earth Science*, *11*(3), 505–514. <https://doi.org/10.1007/s11707-017-0641-4>
- Feld, S. I., Cristea, N. C., & Lundquist, J. D. (2013). Representing atmospheric moisture content along mountain slopes: Examination using distributed sensors in the Sierra Nevada, California. *Water Resources Research*, *49*(7), 4424–4441. <https://doi.org/10.1002/wrcr.20318>
- Flerchinger, G. N., Xaio, W., Marks, D., Sauer, T. J., & Yu, Q. (2009). Comparison of algorithms for incoming atmospheric long-wave radiation. *Water Resources Research*, *45*, 1–14. <https://doi.org/10.1029/2008WR007394>
- Follum, M. L., Downer, C. W., Niemann, J. D., Roylance, S. M., & Vuyovich, C. M. (2015). A

- radiation-derived temperature-index snow routine for the GSSHA hydrologic model. *Journal of Hydrology*, 529(P3), 723–736. <https://doi.org/10.1016/j.jhydrol.2015.08.044>
- Follum, M. L., Niemann, J. D., & Fassnacht, S. R. (2019). A comparison of snowmelt-derived streamflow from temperature-index and modified-temperature-index snow models. *Hydrological Processes*, 33(23), 3030–3045. <https://doi.org/10.1002/hyp.13545>
- Franklin, A. I. (1983). Climate of the Priest River experimental forest, northern Idaho. *USDA Forest Service, Washington, D.C.*
- Garcia, E. S., Tague, C. L., & Choate, J. S. (2013). Influence of spatial temperature estimation method in ecohydrologic modeling in the Western Oregon Cascades. *Water Resources Research*, 49(3), 1611–1624. <https://doi.org/10.1002/wrcr.20140>
- Gardner, A. S., & Sharp, M. (2009). Sensitivity of net mass-balance estimates to near-surface temperature lapse rates when employing the degree-day method to estimate glacier melt. *Annals of Glaciology*, 50(50), 80–86.
- Hamlin, L., Pietroniro, A., Prowse, T., Soulis, R., & Kouwen, N. (1998). Application of indexed snowmelt algorithms in a northern wetland regime. *Hydrological Processes*, 12(10–11), 1641–1657. [https://doi.org/10.1002/\(SICI\)1099-1085\(199808/09\)12:10/11<1641::AID-HYP686>3.0.CO;2-W](https://doi.org/10.1002/(SICI)1099-1085(199808/09)12:10/11<1641::AID-HYP686>3.0.CO;2-W)
- Harlow, R. C., Burke, E. J., Scott, R. L., Shuttleworth, W. J., Brown, C. M., & Petti, J. R. (2004). Derivation of temperature lapse rates in semi-arid south-eastern Arizona Research Note: Derivation of temperature lapse rates in semi-arid south-eastern Arizona. *Hydrology and Earth System Sciences*, 8(6), 1179–1185. <http://edcdaac.usgs.gov/>
- Hock, R. (1999). Including Potential Direct Solar Radiation. *Journal of Glaciology*, 45(149), 101–111.
- Hock, R. (2003). Temperature index melt modelling in mountain areas. *Journal of Hydrology*, 282, 104–115. [https://doi.org/10.1016/S0022-1694\(03\)00257-9](https://doi.org/10.1016/S0022-1694(03)00257-9)
- Immerzeel, W., Petersen, L., Ragettli, S., & Pellicciotti, F. (2014). The importance of observed gradients of air temperature and precipitation for modeling runoff from a glacierized watershed in the Nepalese Himalayas. *Water Resources Research*, 50, 2212–2226. <https://doi.org/10.1002/2013WR014506>
- Immerzeel, W. W., Petersen, L., Ragettli, S., & Pellicciotti, F. (2014). The importance of observed gradients of air temperature and precipitation for modeling runoff from a glacierized watershed in the Nepalese Himalayas. *Water Resources Research*, 50, 2212–2226. <https://doi.org/10.1002/2013WR014506>
- Kampf, S. K., & Richer, E. E. (2014). Estimating source regions for snowmelt runoff in a Rocky Mountain basin: tests of a data-based conceptual modeling approach. *Hydrological Processes*, 28, 2237–2250. <https://doi.org/10.1002/hyp.9751>
- Kimball, J. S., Running, S. W., & Nemani, R. (1997). An improved method for estimating surface humidity from daily minimum temperature. *Agricultural and Forest Meteorology*, 85, 87–98. [https://doi.org/10.1016/S0168-1923\(96\)02366-0](https://doi.org/10.1016/S0168-1923(96)02366-0)

- Kulshrestha, S., Ramsankaran, R., Kumar, A., Arora, M., & Kumar, A. (2018). Investigating the Performance of Snowmelt Runoff Model Using Temporally Varying Near-Surface Lapse Rate in Western Himalayas Estimation of rainfall using satellite Imagery with use of machine learning software WEKA View project Towards a Comprehensive Dat. *Current Science*, *114*(4), 808–813. <https://doi.org/10.18520/cs/v114/i04/808-813>
- Kunkel, K. E. (1989). Simple Procedures for Extrapolation of Humidity Variables in the Mountainous Western United States. *Journal of Climate*, *2*, 656–669.
- Kustas, W. P., Rango, A., & Uijlenhoet, R. (1994). A simple energy budget algorithm for the snowmelt runoff model. *Water Resources Research*, *30*(5), 1515–1527. <https://doi.org/10.1029/94WR00152>
- Li, X., & Williams, M. W. (2008). Snowmelt runoff modelling in an arid mountain watershed, Tarim Basin, China. *Hydrological Processes*, *22*, 3931–3940. <https://doi.org/10.1002/hyp>
- Liston, G. E., & Elder, K. (2006). A distributed snow-evolution modeling system (snowmodel). *Journal of Hydrometeorology*, *7*(6), 1259–1276. <https://doi.org/10.1175/JHM548.1>
- Lundquist, J. D., & Cayan, D. R. (2007). Surface temperature patterns in complex terrain: Daily variations and long-term change in the central Sierra Nevada, California. *Journal of Geophysical Research Atmospheres*, *112*(11), 1–15. <https://doi.org/10.1029/2006JD007561>
- Lute, A. C., & Abatzoglou, J. T. (2020). Best practices for estimating near-surface air temperature lapse rates. *International Journal of Climatology*, *November 2019*, 1–16. <https://doi.org/10.1002/joc.6668>
- Martinec, J., & Rango, A. (1986). Parameter values for snowmelt runoff modelling. *Journal of Hydrology*, *84*(3–4), 197–219. [https://doi.org/10.1016/0022-1694\(86\)90123-X](https://doi.org/10.1016/0022-1694(86)90123-X)
- Minder, J. R., Mote, P. W., & Lundquist, J. D. (2010). Surface temperature lapse rates over complex terrain: Lessons from the Cascade Mountains. *Journal of Geophysical Research Atmospheres*, *115*(14), 1–13. <https://doi.org/10.1029/2009JD013493>
- Misra, A., Kumar, A., Bhambri, R., Haritashya, U. K., Verma, A., Dobhal, D. P., Gupta, A. K., Gupta, G., & Upadhyay, R. (2020). Topographic and climatic influence on seasonal snow cover: Implications for the hydrology of ungauged Himalayan basins, India. *Journal of Hydrology*, *585*(April 2019), 124716. <https://doi.org/10.1016/j.jhydrol.2020.124716>
- Navarro-Serrano, F., López-Moreno, J. I., Azorin-Molina, C., Alonso-González, E., Tomás-Burguera, M., Sanmiguel-Vallelado, A., Revuelto, J., & Vicente-Serrano, S. M. (2018). Estimation of near-surface air temperature lapse rates over continental Spain and its mountain areas. *International Journal of Climatology*, *38*(8), 3233–3249. <https://doi.org/10.1002/joc.5497>
- Ohmura, A. (2001). Physical basis for the temperature-based melt-index method. *Journal of Applied Meteorology*, *40*(4), 753–761. [https://doi.org/10.1175/1520-0450\(2001\)040<0753:PBFTTB>2.0.CO;2](https://doi.org/10.1175/1520-0450(2001)040<0753:PBFTTB>2.0.CO;2)
- Pagano, T., Garen, D., & Sorooshian, S. (2004). Evaluation of official western U.S. seasonal water supply outlooks, 1922-2002. *Journal of Hydrometeorology*, *5*(5), 896–909. [https://doi.org/10.1175/1525-7541\(2004\)005<0896:EOOWUS>2.0.CO;2](https://doi.org/10.1175/1525-7541(2004)005<0896:EOOWUS>2.0.CO;2)

- Rango, A., & Martinec, J. (1996). Revisiting the Degree-Day Method for. *Water Resources Bulletin*, 31(4).
- Richard, C., & Gratton, D. J. (2001a). The importance of the air temperature variable for the snowmelt runoff modelling using the SRM. *HYDROLOGICAL PROCESSES Hydrol. Process*, 15, 3357–3370. <https://doi.org/10.1002/hyp.1031>
- Richard, C., & Gratton, D. J. (2001b). The importance of the air temperature variable for the snowmelt runoff modelling using the SRM. *Hydrological Processes*, 15(18), 3357–3370. <https://doi.org/10.1002/hyp.1031>
- Rolland, C. (2003). Spatial and seasonal variations of air temperature lapse rates in alpine regions. *Journal of Climate*, 16(7), 1032–1046. [https://doi.org/10.1175/1520-0442\(2003\)016<1032:SASVOA>2.0.CO;2](https://doi.org/10.1175/1520-0442(2003)016<1032:SASVOA>2.0.CO;2)
- Ruckstuhl, C., Philipona, R., Morland, J., & Ohmura, A. (2007). Observed relationship between surface specific humidity, integrated water vapor, and longwave downward radiation at different altitudes. *Journal of Geophysical Research Atmospheres*, 112, 1–7. <https://doi.org/10.1029/2006JD007850>
- Running, S. W., & Ramakrishna, R. N. (1987). Extrapolation of synoptic meteorological data in mountainous terrain and its use for simulating forest evapotranspiration and photosynthesis. *Can. J. For. Res.*, 17, 472–483.
- Schneider, D., & Molotch, N. (2016). Real-time estimation of snow water equivalent in the Upper Colorado River Basin using MODIS-based SWE Reconstructions and SNOTEL data. *Water Resources Research*, 52, 7892–7910. <https://doi.org/10.1002/2016WR019067>
- Sexstone, G. A., & Fassnacht, S. R. (2014). What drives basin scale spatial variability of snowpack properties in northern Colorado? *Cryosphere*, 8(2), 329–344. <https://doi.org/10.5194/tc-8-329-2014>
- Shen, Y. J., Shen, Y., Goetz, J., & Brenning, A. (2016). Spatial-temporal variation of near-surface temperature lapse rates over the Tianshan mountains, central Asia. *Journal of Geophysical Research*, 121(23), 14,006–14,017. <https://doi.org/10.1002/2016JD025711>
- Sicart, J., J., P., Essery, R., & Bewley, D. (2006). Incoming longwave radiation to melting snow: observations, sensitivity and estimation in northern environments. *Hydrological Processes*, 20, 3697–3708. <https://doi.org/10.1002/hyp.6383>
- Sospedra-Alfonso, R., Melton, J. R., & Merryfield, W. J. (2015). Effects of temperature and precipitation on snowpack variability in the Central Rocky Mountains as a function of elevation. *Geophysical Research Letters*, 42(11), 4429–4438. <https://doi.org/10.1002/2015GL063898>
- Tercek, M. T., Rodman, A., Woolfolk, S., Wilson, Z., Thoma, D., & Gross, J. (2021). Correctly applying lapse rates in ecological studies: comparing temperature observations and gridded data in Yellowstone. *Ecosphere*, 12(3). <https://doi.org/10.1002/ecs2.3451>
- Wang, L., Sun, L., Shrestha, M., Li, X., Liu, W., Zhou, J., Yang, K., Lu, H., & Chen, D. (2016). Improving snow process modelign with satellite-bsaed estimation of near-surface-air temperatute lapse rate. *Journal of Geophysical Research Atmospheres*, 121(12), 5–30.

<https://doi.org/10.1002/2016JD025506>.

- Webb, R. W., Fassnacht, S. R., & Gooseff, M. N. (2017). DEFINING THE DIURNAL PATTERN OF SNOWMELT USING A BETA DISTRIBUTION. *Journal of the American Water Resources Association*, 53(3), 684–696. <https://doi.org/10.1111/1752-1688.12522>
- Whiteman, C., Zhong, S., Shaw, W., Hubbe, M., Bian, X. (2001). Cold Pools in the Columbia Basin. *Weather and Forecasting*, 16(4), 432-447.
- Wigmosta, M. S., Vail, L. W., & Lettenmaier, D. P. (1994). A distributed hydrology-vegetation model for complex terrain. *Water Resources Research*, 30(6), 1665–1679. <https://doi.org/10.1029/94WR00436>
- Zhang, F., Zhang, H., Hagen, S. C., Ye, M., Wang, D., Gui, D., Zeng, C., Tian, L., & Liu, J. (2015). Snow cover and runoff modelling in a high mountain catchment with scarce data: effects of temperature and precipitation parameters. *Hydrological Processes*, 29(1), 52–65. <https://doi.org/10.1002/hyp.10125>

## CHAPTER 2. RESEARCH INVESTIGATION

### 2.1 Introduction

Across the western US, water supply forecasts are made through regressions between historical runoff volumes or SWE measured at snow course and SNOTEL stations (Pagano et al., 2004; Schneider & Molotch, 2016). However, data (e.g., air temperature, dew point temperature, relative humidity, snow depth, SWE, etc.) are often collected at different scales than those needed for forecasting (Blöschl, 1999). In mountainous regions, a majority of snowmelt occurs at high elevation where there are few hydrometeorological measurements to monitor snowpack processes (Minder et al., 2010). Due to this lack of hydrometeorological measurements, data (i.e., air temperature and dew point temperature) are often extrapolated based on points measurements and elevation (Blandford et al., 2008; Collados-Lara et al., 2021; Harlow et al., 2004; Immerzeel et al., 2014; Lundquist & Cayan, 2007; Lute & Abatzoglou, 2020; Navarro-Serrano et al., 2018; Rolland, 2003; Shen et al., 2016). Such extrapolated near-surface air temperatures are commonly applied in hydrologic models (Garcia et al., 2013; Immerzeel et al., 2014; Kampf & Richer, 2014; Kulshrestha et al., 2018; Minder et al., 2010; Misra et al., 2020; Wang et al., 2016; Zhang et al., 2015).

Generally, the change of temperature with elevation in the free atmosphere, known as the environmental lapse rate (ELR), averages about  $-6.5$  °C/km (Barry & Chorley, 1987). In practice, the ELR is used to represent the change in near-surface temperature-elevation gradient (TEG). As indicated by the negative sign of the ELR, temperatures typically decrease with increasing elevation. However, in some time periods and locations temperature increases with elevation, due to cold air drainage and pooling (Collados-Lara et al., 2021; Follum et al., 2015; Lundquist

& Cayan, 2007; Navarro-Serrano et al., 2018; Rolland, 2003). Additionally, the air temperature-elevation gradient varies temporally (seasonally and diurnally) and geographically (Blandford et al., 2008; Collados-Lara et al., 2021; Lundquist & Cayan, 2007; Lute & Abatzoglou, 2020; Navarro-Serrano et al., 2018; Rolland, 2003; Shen et al., 2016). Although there is a general understanding of TEG and the governing processes (e.g., radiative processes and atmospheric dynamics), estimating and applying to hydrologic, meteorological, snowpack modeling remains difficult due to microscale temperature variability.

Dew point temperatures represent atmospheric moisture content and are essential for modeling the water balances and partially energy balances. Dew point temperature, which is a surrogate for vapor pressure, influences both incoming longwave radiation and latent heat flux (Ruckstuhl et al., 2007). Incoming longwave radiation is a function of air temperature, water vapor (Flerchinger et al., 2009), cloud cover, and other atmospheric conditions. Higher dew point temperatures increase incoming longwave radiation since water vapor raises the emissivity of the atmosphere (Rangwala et al., 2010). Additionally, a smaller difference between air and dew point temperature results in reduced evaporation or sublimation. Despite its importance to the water cycle, atmospheric moisture is seldom measured (Feld et al., 2013). Similar to air temperature, extrapolation from lower elevations is often used to estimate dew point temperatures (Feld et al., 2013). Additionally, the gradients are generally negative, meaning a decrease in dew point temperature as elevation increases. Kunkel (1989) estimated the dew point temperature-elevation gradient (DTEG) to be an average of  $-5.1$  °C/km over the months of May and June.

Due to its computational simplicity, snowmelt modeling often uses a temperature index method due to its satisfactory performance and the wide availability of air temperature data

(Hock, 2003; Ohmura, 2001). Such models are valuable to simulate snowmelt since temperature and precipitation are the only forcing variables (Hock, 2003). Studies have added radiation components to temperature-index models to account for energy processes that are typically dominant controls on snowmelt rates, especially in mid-latitudes (Brubaker et al., 1996; Cazorzi & Dalla Fontana, 1996; Dunn & Colohan, 1999; Follum et al., 2015; Hamlin et al., 1998; Hock, 1999; Rango & Martinec, 1996). The addition of radiation components into the temperature index model can yield more accurate snowmelt outputs mostly due to the increase in net shortwave radiation as the melt season progresses (Follum et al., 2015, 2019; Hamlin et al., 1998; Kustas et al., 1994).

Studies have explored the impacts of variable TEG and DTEG, and their sensitivity in modeling (Feld et al., 2013; Garcia et al., 2013; Gardner & Sharp, 2009; Immerzeel et al., 2014; Kampf & Richer, 2014; Li & Williams, 2008; Martinec & Rango, 1986; Minder et al., 2010; Richard & Gratton, 2001; Tercek et al., 2021; Wang et al., 2016; Zhang et al., 2015). A study in the Cascade Range of Oregon determined that snowmelt was most delayed when the ELR was used compared to weather stations and temperature modeled from the PRISM dataset (Garcia et al., 2013). Using 200 m elevation zones in the Washington Cascades, Minder et al. (2010) found that the modeled snowmelt shifted a full month earlier when the lapse rate was changed from -6.5 °C/km to -4.0 °C/km. The sensitivity of the TEG values used produced a 15 to 62% difference in simulated discharge amount (Wang et al., 2016; Zhang et al., 2015).

Two studies within the Cache la Poudre basin focused on TEG (Collados-Lara et al., 2021; Kampf & Richer, 2014). Collados-Lara et al. (2021) found that at the fine-scale (10s of meters verticals over 100s of meters) the temperature-elevation gradients were positive, often an order of magnitude larger than coarse (one measurement every 15 km) scale TEGs, while Kampf and

Richer (2014) adjusted the TEG from -6.0 to -9.0, with a baseline of -8.0 °C/km to model snowmelt runoff and found minimal differences in snowmelt. Using techniques and background information from previous local studies, we focused on a finer spatial scale and the impacts that TEG and DTEG have on modeling snowmelt over an 8.8 km<sup>2</sup> watershed. This study will inform water managers whether widely used temperature-elevation gradients are accurately estimating snowmelt by comparing a dense network of temperature sensors to estimated values and their impacts on snowmelt. In addition to understanding the importance of TEG and DTEG on snowmelt, this study is essential because it is located nearby the Cameron Peak Fire, which burned over 200,000 acres, and is the largest fire in Colorado history (US Forest Service InciWeb). Understanding TEG and DTEG in subalpine to alpine environments within the Cache la Poudre can contribute to the extensive ongoing to understand wildfire impacts, especially in the persistent snow zone.

In this study, we compute TEG and DTEG and compare to widely accepted rates used for temperature extrapolation (Barry & Chorley, 1987; Kunkel, 1989; Liston & Elder, 2006). The influence of season, aspect, time of day, and wind speed are utilized to understand TEG and DTEG patterns. Additionally, the implications on snowmelt modeling of TEG and DTEG versus accepted temperature-elevation gradients are quantified. A variety of methods using the temperature and radiation index model is completed to understand the influence air temperature and dew point temperature (as a surrogate of vapor pressure) have on snowmelt. This research poses the following questions: (1) how does TEG vary temporally and spatially compared to values in literature, and can this variability be explained from other meteorological variables, (2) how does DTEG vary temporally and spatially compared to values in literature, and can this

variability be explained from other meteorological variables, (3) how do observed and published TEG and DTEG affect snowmelt modeling.

## **2.2 Study Area and Datasets**

### *2.2.1 Joe Wright Creek Study Area*

Joe Wright Creek above Joe Wright Reservoir (JWC; USGS gauge number 06746095), is located within the Cache la Poudre River basin in north-central Colorado (Figure 2-1). It is an 8.8 km<sup>2</sup> snowmelt-dominated watershed ranging in elevation from 3,041 to 3,673 m, with an average elevation of 3,288 m. The watershed slopes range from 0 to 56 degrees with an average of 16 degrees with dominant aspects being east, southeast, and northwest. It flows into Joe Wright Reservoir, constructed to receive water added from the Michigan Ditch, a trans-basin water diversion from the Michigan River. JWC consists of subalpine forest (approximately 60%), mainly coniferous, and alpine tundra (approximately 40%). Within the alpine and subalpine, 20.4% is perennial snow/ice, 0.1% developed, 9.1% barren land, 60.8% evergreen forest, 9.6% herbaceous, and 0.1% woody wetlands (USGS National Land Cover Database, accessed September 15, 2021).

The Natural Resources Conservation Service (NRCS) Joe Wright snow telemetry (SNOTEL) station <<https://www.wcc.nrcs.usda.gov>>, located near the center of JWC watershed (Figure 2-1), measures SWE, precipitation, air temperature (since 1998) and snow depth (since 2004). Air temperature, precipitation, snow depth, and SWE. In addition to the SNOTEL station, the Cameron Pass Colorado Avalanche Information Center (CAIC) meteorological station is located 2 km south of JWC (Figure 2-1). It has been in operation since 2011 and measures temperature, relative humidity, dew point temperature, wind speed, wind directions, snow depth,

incoming and outgoing shortwave radiation, incoming and outgoing longwave radiation, and net radiation.

Based on Joe Wright Snow Telemetry (SNOTEL) data, from water years (WY) 1980 to 2020, the average annual peak SWE was 672 mm, on average occurring May 1<sup>st</sup> (ranging from March 9 to June 1), and average complete melt out date (i.e., first day during melt that SWE equals 0 mm) was June 17<sup>th</sup> (ranging from May 15 to July 11). Melt generally occurs between April and June at JWC when the average air temperature is 5.56 °C. The average annual accumulated precipitation was 1,129 mm (<<https://www.wcc.nrcs.usda.gov>>, accessed September 15, 2021).

The study focuses on May and June 2020 and 2021 since snowmelt predominantly occurs between these two months. Figure 2-2 provides hourly air and dew point temperature for this period. The air temperature for both years during May and June generally ranges between -5 to 25 °C. The air temperature in June 2021 is greater than June 2020 (Figure 2-2). The dew point temperature generally ranges between -15 to 10 °C (Figure 2-2). Wind rose diagrams are presented in Figure 2-3 for May and June 2020 and 2021. The wind speeds are greater in 2020 and in both years the dominant wind direction is the southwest (Figure 2-3).

In addition to the CAIC radiation data, an anemometer from the CAIC weather station was used to determine hourly wind speed and direction. A wind rose for May and June 2020 and 2021 are presented in Figure 2-3. As shown in Figure 2-3, wind direction is most often from the southwest.

### 2.2.2 *Field Datasets*

A network, totaling 16 to 18 sensors, of Blue Maestro Tempo Disc <sup>TM</sup> sensors (<<http://www.bluemaestro.com>>, accessed September 15, 2021), herein referred to as BM

sensors, were installed on a west and east transect of JWC ranging in elevation from 3,051 to 3,453 m to measure hourly temperature and relative humidity (Figure 2-1). The temperature sensors were installed in April and May 2020 with a few additional sensors added in April 2021. Four snow surveys were conducted in May and June 2021 collecting snow depth, SWE, and bulk density measurements within and near JWC based on elevation (Figure 2-1). Their location was recorded with a hand-held GPS unit.

### 2.2.3 *Spatial Datasets*

The USGS National Land Cover Database was used for JWC and surrounding areas (<https://datagateway.nrcs.usda.gov>). The land cover map utilized includes 30 m by 30 m pixels. The land cover map was used to depict forested versus unforested land. A DEM extracted from the USDA NRCS website was utilized to determine elevations of the BM sensors. The resolution of the DEM was 10 m by 10 m (<https://datagateway.nrcs.usda.gov>, accessed July 1, 2021).

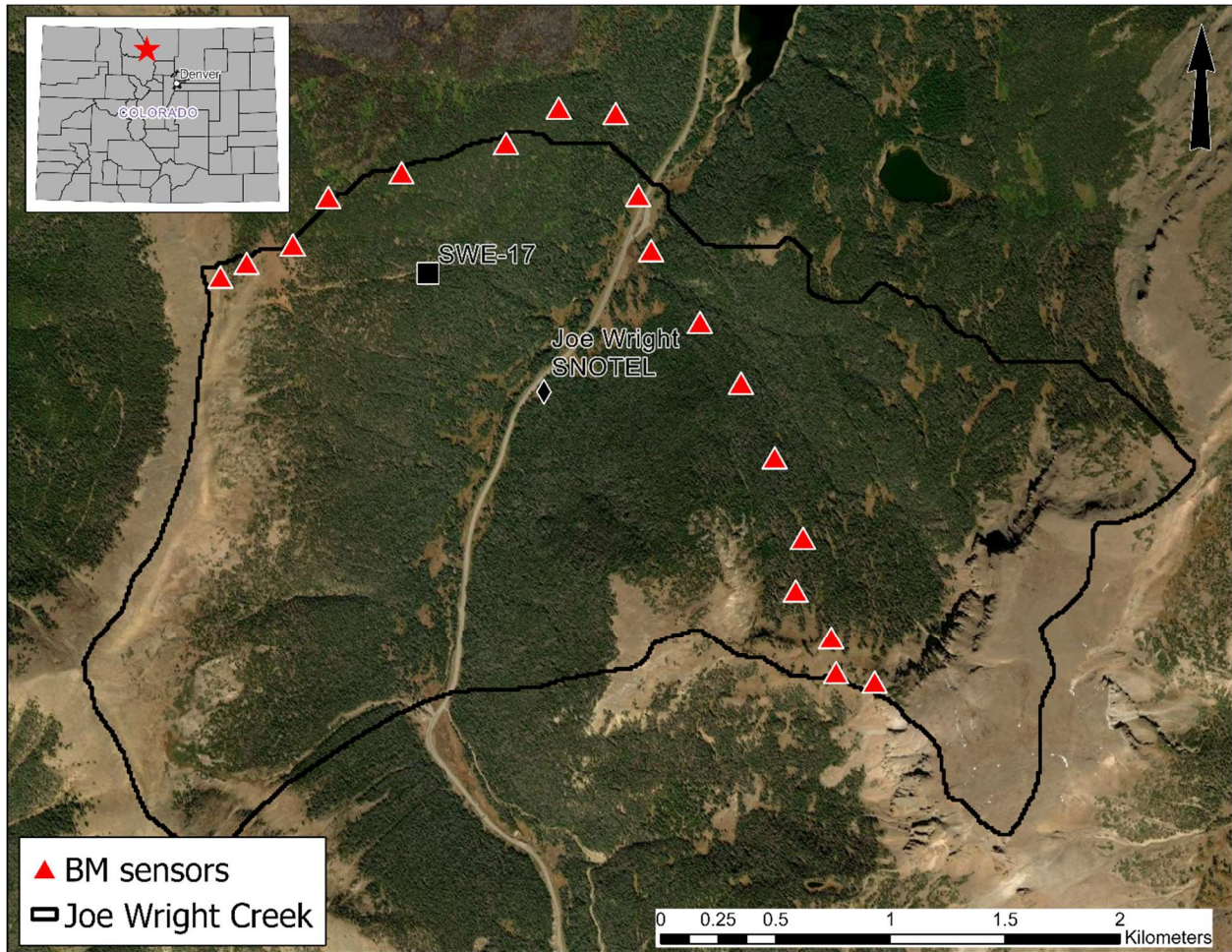


Figure 2-1. Map of Joe Wright Creek (JWC) study area. The triangles represent temperature and RH sensors. The diamonds represent the Joe Wright SNOTEL and Cameron Pass CAIC station.

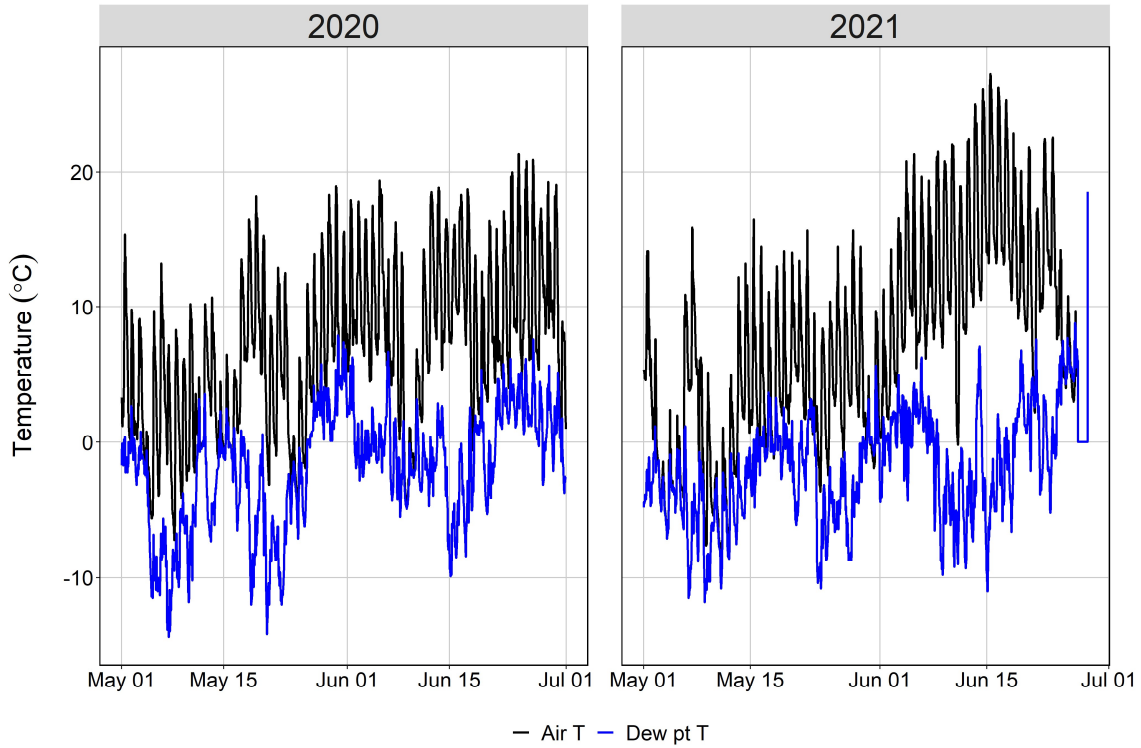


Figure 2-2. Joe Wright hourly air and dew point temperature for May and June 2020 and 2021.

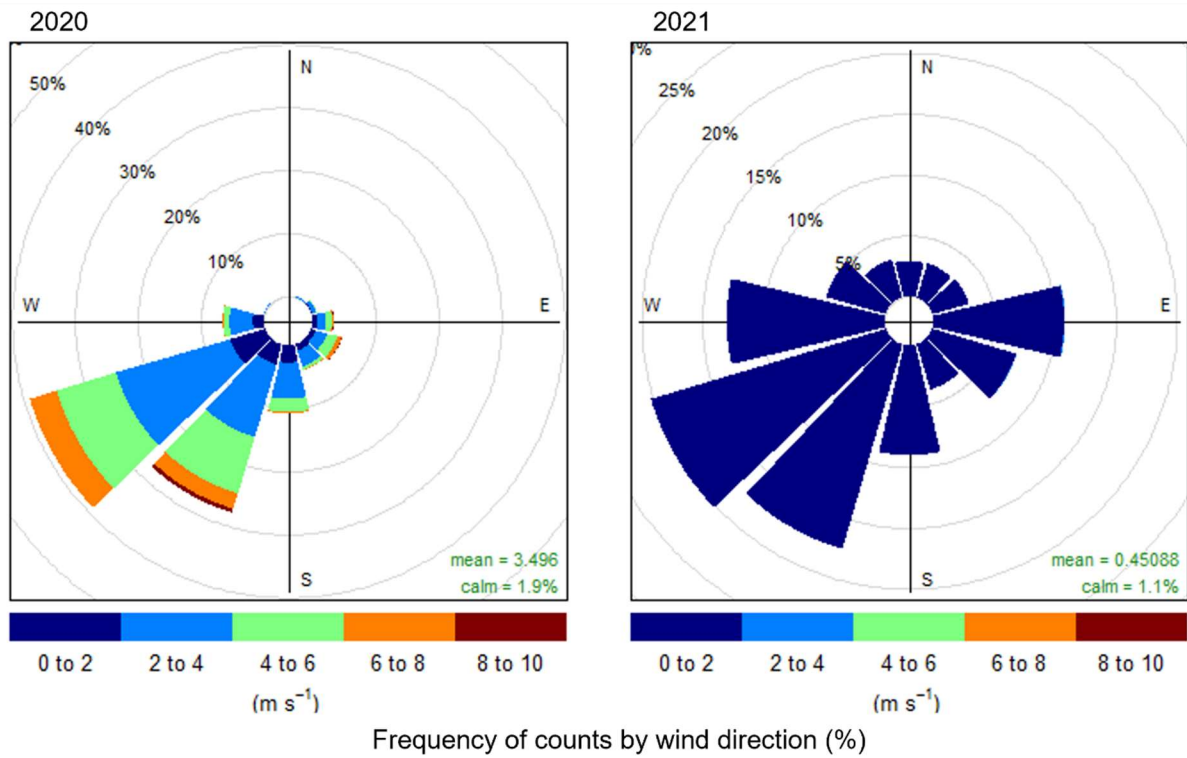


Figure 2-3. Wind rose from the CAIC Cameron Pass weather station for May and June 2020 and 2021.

## 2.3 Methodology

### 2.3.1 *Temperature and dew point temperature elevation gradients*

While the temperature and relative humidity sensors collected hourly data continuously from April 2020 to June 2021, the focus was on the snowmelt seasons (i.e., May through June). The BM sensors were installed with alternative double funnel systems with air holes for flow (Hubbart, 2011) and attached on the north side of evergreen trees to reduce direct solar loading (Lundquist & Huggett, 2008) at approximately 2-m above ground surface, as per Collados-Lara et al. (2021) and Kingston et al. (in review). Snow accumulation causes the height of the sensor above the snow to decrease, which could affect the temperature measurement. However, snow accumulation and ablation are generally uniform across the domain. On each transect, the BM sensors were placed every 50 m of elevation gain (Figure 2-1). The sensor temperature accuracy (air and dew point) is generally within 0.3 °C of the actual temperature and a resolution of 0.1 °C, while the humidity accuracy is generally within 3% with a maximum uncertainty of 4% <bluemaestro.com>.

The air temperature time series were assessed graphically to identify obvious outliers from the range of air temperature across all sensors for each time step. A range threshold of 20 °C was used to further identify possible outliers, since most of the ranges for hourly time steps fell within this range. If a 20 °C range was identified for a time step, the data from each sensor were compared to the measurements from the previous and subsequent time steps. Outliers at individual sensors were due to two factors: a sensor was being installed at that time step which was usually warmer than the ambient air, or a sensor was beginning to drift due to a low battery and shut down shortly after the drift began. Data identified as outliers were removed from the dataset.

For each time step, the hourly TEG was computed as the slope of the temperature versus elevation. Additionally, coefficient of determination ( $R^2$ ) values, and the significance of the correlation were determined per Collados-Lara et al. (2021a). To better understand TEG patterns, TEG were examined over each melt snowmelt season, daily and nightly, and by transect (west versus east). Additionally, daily averages were computed. During the snowmelt period, daytime hours represented 08:00 and 18:00 and nighttime hours were 17:00 to 07:00 of the next day. These time frames were selected by evaluating the TEG quantities when they were negative, positive, and averaging when those changes occur.

Dew point temperature ( $T_d$ ) was used to evaluate observed vapor pressure gradients with elevation, in a similar manner as air temperature. To determine vapor pressure ( $e_a$ ), the following equation (Dingman, 2015) was used:

$$e_a = 6.112 \times \exp^{\frac{(a \times T_d)}{b + T_d}} \quad (\text{Equation 2-1}),$$

where  $a$  is a constant equal to 17.62,  $b$  is a temperature constant equal to 243.12 (World Meteorological Organization, 2008). Equation 2-1 can be applied since dew point temperature is the temperature at which the vapor pressure is saturated.

An anemometer from the CAIC weather station was used to determine hourly wind speed and direction. A wind rose for May and June 2020 and 2021 are presented in Figure 2-3. The wind speed and direction values were utilized to understand the relationship between such measurements and TEG and DTEG. The wind speed data were classified into one m/s wind speed bins when used to compare wind speed and temperature-elevation gradients.

### 2.3.2 *Observed SWE and snowmelt*

SWE was measured using a Snow-Hydro coring tube <snowhydro.com> throughout the 2021 melt season (Figure 2-1 and Table A-2). Three snow cores were taken from each sampling location, and results were averaged. For each snow core, depth was measured, and mass of snow was recorded; SWE was computed using the mass of snow and the known volume of the coring tube. At each repeated SWE measurement location, it was noted whether the canopy was open or closed (Fassnacht et al., 2017). The repeated SWE measurements were combined with fresh snow added from Joe Wright SNOTEL with an applied precipitation gradient (Liston & Elder, 2006) to understand the change of SWE during the melt season for application of the snowmelt model. SWE measurements at the highest elevation, with the most repeated measurements, and an open canopy (similar to Joe Wright SNOTEL) were used to investigate the accuracy of the snowmelt model (further discussed in Section 2.3.3).

### 2.3.3 *Snowmelt modeling*

To capture the sensitivity of TEG and vapor pressure (a surrogate for DTEG) on snowmelt, scenarios were run using different temperature and/or vapor pressure values depending on the modeling equation (Table 2-1). The scenarios used a combination of observed temperature, temperature computed using the ELR (-6.5 °C/km; applied to the SNOTEL data), temperature computed using the Liston and Elder (2006) air temperature lapse rate (-8.15 °C/km), observed vapor pressure, and lapsed vapor pressure from a BM sensor (similar in elevation to the Joe Wright SNOTEL since RH is not provided with SNOTEL data) using the Kunkel (1989) dew point temperature lapse rate (-5.1 °C/km). Model scenarios are identified in Table 2-1. Snowmelt was determined at a paired BM sensor and snow sampling location beginning on May 1, 2021 to the melt out date.

### 2.3.3.1 Temperature index modeling

The temperature index model computed melt (M) as a function of air temperature ( $T_a$ ):

$$M = MF_{Ti} (T_a - T_{oi}) \quad (\text{Equation 2-2}),$$

where M represents the melt water per unit time,  $MF_{Ti}$  is temperature melt factor,  $T_a$  is the air temperature per unit time, and  $T_{oi}$  is the reference temperature. Equation 2-2 was run using variable melt factors from Fassnacht et al. (2017); a continuous set of melt factors was not available for the Joe Wright SNOTEL station so the  $MF_{Ti}$  values from the nearby Lake Irene SNOTEL station were used. The continuous melt factors from Fassnacht et al. (2017) are presented in the appendix. For the temperature index model, the reference temperature was set to 0 °C. In Table 2-1, these are obs T & simpler model and local lapse T & simpler model. The temperature index model was run to evaluate its performance compared to the temperature and radiation index model.

### 2.3.3.2 Temperature and radiation index modeling

The temperature and radiation index modeling equation is utilized in the first five scenarios in Table 2-1. This model builds on the temperature index model (equation 2-2) by adding net shortwave ( $H_K^*$ ) and longwave ( $H_L^*$ ) radiation, as follows:

$$M = MF_{Ti}(T_a - T_{oi}) + MF_{Hi}(H_K^* + H_L^*) \quad (\text{Equation 2-3}),$$

where  $MF_{Hi}$  is a radiation melt factor, and  $H_K^* + H_L^*$  represent net radiation (Hamlin et al., 1998). A radiation melt factor was determined for non-vegetated areas. The melt factors and reference temperature were optimized using a nonlinear optimization approach with observed snowmelt for the 2021 season (i.e., from the Joe Wright SNOTEL). The reference temperature was assumed to be constant at 4.58 °C based on the optimization from melt at the Joe Wright

SNOTEL. The snowmelt model was run on a daily time step and hourly temperatures above 4.58 °C were summed for each day. Similarly, hourly net radiation was summed per day. Using the same optimization technique as the reference temperature, the  $MF_{Ti}$  value was 1.77 and the  $MF_{Hi}$  was 0.15.

The Kunkel (1989) dew point temperature lapse rate (-5.1 °C/km) was derived using a vapor pressure coefficient ( $0.37 \text{ m}^{-1}$ ) and the temperature constant (a), and a dimensionless constant (b) used in equation 2-4 (WMO, 2008). Using the observed dew point temperature ( $T_d$ ) from a BM sensor,  $T_d$  lapsed to the same elevation as the point snowmelt model elevation (model scenarios obs T & lapse  $T_d$  and local lapse T &  $T_d$ ). The vapor pressure, air temperature, and cloud cover are used to compute the incoming longwave radiation (Equation 2-4) with temperature and cloud cover to compute the effective atmospheric emissivity (Equation 2-5), which are covered in detail below.

A four-component radiometer (incoming shortwave, outgoing shortwave, incoming longwave, and outgoing longwave) was installed at the Joe Wright SNOTEL during the winter of 2021. However, due to datalogger failure, the dataset is limited and could not be utilized for this study. Therefore, the four-component radiometer data from the CAIC Cameron Pass – meteorological station were used for snowmelt modeling. The limited radiation data from the Joe Wright SNOTEL were compared to the CAIC radiation data to determine the similarity of the data. Each radiation component from both stations were plotted together to determine suitability.

Although radiation variables are not uniform in a mountain watershed, the incoming shortwave, outgoing shortwave, and outgoing longwave radiations were assumed to be consistent across JWC (Follum et al., 2015). However, the incoming longwave radiation ( $H_{L-in}$ ) was assumed to vary spatially by elevation as a function of temperature and vapor pressure.

Assuming that the cloud cover was similar between the CAIC station and across JWC (Follum et al., 2015), the CAIC incoming longwave radiation was used to estimate cloud cover, similar to the approach of Fassnacht et al. (2001) who used daytime shortwave radiation for this purpose.

The incoming longwave radiation ( $H_{L-in}$ ) can be computed as follows:

$$H_{L-in} = \epsilon_{atmos} \sigma T_a^4 \quad (\text{Equation 2-4}),$$

where  $\epsilon_{atmos}$  is the effective atmospheric emissivity,  $\sigma$  is the Stefan-Boltzman constant ( $5.67 \times 10^{-8} \text{ W/m}^2/\text{K}^4$ ), and  $T_a$  is observed air temperature in degrees Kelvin (Dingman, 2015). The effective atmospheric emissivity in Equation 2-4 can be computed as a function of cloud cover ( $C_{cloud}$ ):

$$\epsilon_{atmos} = (0.53 + 0.065e_a)(1 + 0.4C_{cloud}) \quad (\text{Equation 2-5}),$$

where  $e_a$  represents vapor pressure (Dingman, 2015).

Since the CAIC outgoing shortwave radiation was unrealistically low (a maximum of 400  $\text{W/m}^2$ ) for melt season 2021, albedo was modeled using the Joe Wright SNOTEL data to identify the occurrence of snowfall, simulate albedo decay after snowfall, and use albedo to determine net shortwave radiation. The first order decay model was used to estimate albedo of snow ( $\alpha_s$ ) (U.S. Army Corps of Engineers, 1956):

$$\alpha_s = [\alpha_{s(t-1)} - \alpha_{s-min}]e^{-k\Delta t} + \alpha_{s-min} \quad (\text{Equation 2-6}),$$

where  $k$  is a decay coefficient (set to 0.01 per hour, as per Verseghy, 1991), and  $\Delta t$  is the time step in hours. An albedo minimum value ( $\alpha_{s-min}$ ) of 0.5 was used if the snowpack was melting ( $T_a > 0 \text{ }^\circ\text{C}$ ) and 0.7 when melt was not occurring ( $T_a \leq 0 \text{ }^\circ\text{C}$ ). For time steps with fresh snow, which was determine as a positive precipitation value and an increase in snow depth at the SNOTEL

station, the albedo was reset to 0.84 (Verseghy, 1991). The net shortwave radiation was computed as the product of incoming shortwave radiation and one minus albedo.

Table 2-1. Model scenarios to understand sensitivity of air temperature and vapor pressure in snowmelt modeling

<b>Model</b>	<b>Air Temperature (T)</b>	<b>Dew point temperature (T<sub>d</sub>)</b>
obs T	Observed	Observed
ELR T	ELR	Observed
local lapse T	Liston and Elder (2006) T lapse rate	Observed
obs T & lapse T <sub>d</sub>	Observed	Kunkel (1989) T <sub>d</sub> lapse rate
local lapse T & T <sub>d</sub>	Liston and Elder (2006) T lapse rate	Kunkel (1989) T <sub>d</sub> lapse rate
obs T & simpler model	Observed	N/A
local lapse T & simpler model	Liston and Elder (2006) T lapse rate	N/A

## 2.4 Results

### 2.4.1 Observed air temperature and TEG

The TEG values are determined by assessing the air temperature over an elevation gradient over time. Figure 2-2 provides an example of air temperature differences over elevation in the early morning and afternoon on the same date. As shown in Figure 2-2, there is an increase in air temperature with elevation on May 21, 2021 at 05:00, which would produce a positive TEG. Conversely, there is a decrease in air temperature with elevation on May 21, 2021 at 14:00, which would produce a negative TEG. The TEG values predominantly range between -20 to 20 °C/km (Figure 2-5). Generally, correlations are poor at TEG values approaching 0 °C/km with R<sup>2</sup> values less than 0.25 (grey points in Figure 2-5). For positive TEG values, a stronger correlation was observed where TEG values were between 10 to 20 °C/km. Overall, the strongest correlations were observed near the ELR or TEG values less than -5 °C/km. For snowmelt season 2020, the TEG values were variable throughout the whole season, whereas, in 2021, the month

of May had fewer positive TEG values than the rest of the dataset (Figure 2-5). Similar temporal patterns and ranges of TEG values were observed when the years were separated by transect (Figure 2-6). However, the average  $R^2$  value improved when parsed by transect, with an average  $R^2$  of 0.45 for each transect compared to an average  $R^2$  value of 0.33 when combined (Table 2-2). For a specific year, transect, or a combination thereof, the average TEG values were mostly negative and ranged from -2.9 to 0.9 °C/km (Table 2-2). Figure 2-7 shows that TEG is often positive between hours late PM and early AM hours. Conversely, TEG values are generally most negative between hours late AM and early PM hours. The  $R^2$  values based on time of day are variable and indicate no clear correlation between air temperature and elevation, beyond having stronger correlations for larger values (positive or negative), was observed (Figure 2-7).

Since hourly TEG was variable, average daily and average hourly TEG were computed (Figure 2-8) between May and June. When excluding TEG values with an  $R^2$  less than 0.2, the daily median TEG ranges from -8.7 to 13.8 °C/km with an average  $R^2$  of 0.37 (Figure 2-8). Few daily TEG values have a  $R^2$  greater than 0.5 (only 11 percent), but such values range from -7.6 to -4.7 °C/km. Therefore, when the correlation between elevation and near-surface air temperature is stronger, the observed TEG values were similar to the ELR and Liston and Elder (2006) TEG. Additionally, when TEG is evaluated by average hourly value (Figure 2-8), the TEG are positive at night (from hours 00:00 to 07:00 and 21:00 to 23:00), and hourly average TEG values are negative during the day (from 08:00 to 20:00; Figure 2-8), which is similar to the hourly trends seen in Table 2-3 and Figure 2-7.

Excluding TEG values with an  $R^2$  less than 0.2, the positive and negative TEG values were evaluated in 1 m/s wind speed bins (Figure 2-9). Overall, wind speed was greater in 2020 than 2021. For the maximum wind speed bins for both 2020 and 2021 (8 to 9 m/s and 4 to 5 m/s,

respectively), the TEG values are only negative, and the average TEG for wind speeds faster than 4 m/s is  $-5.10\text{ }^{\circ}\text{C}/\text{km}$ . Conversely, the average TEG for wind speeds slower than 4 m/s is  $0.03\text{ }^{\circ}\text{C}/\text{km}$ . However, wind speeds less than 4 m/s account for 83 percent of the measurements.

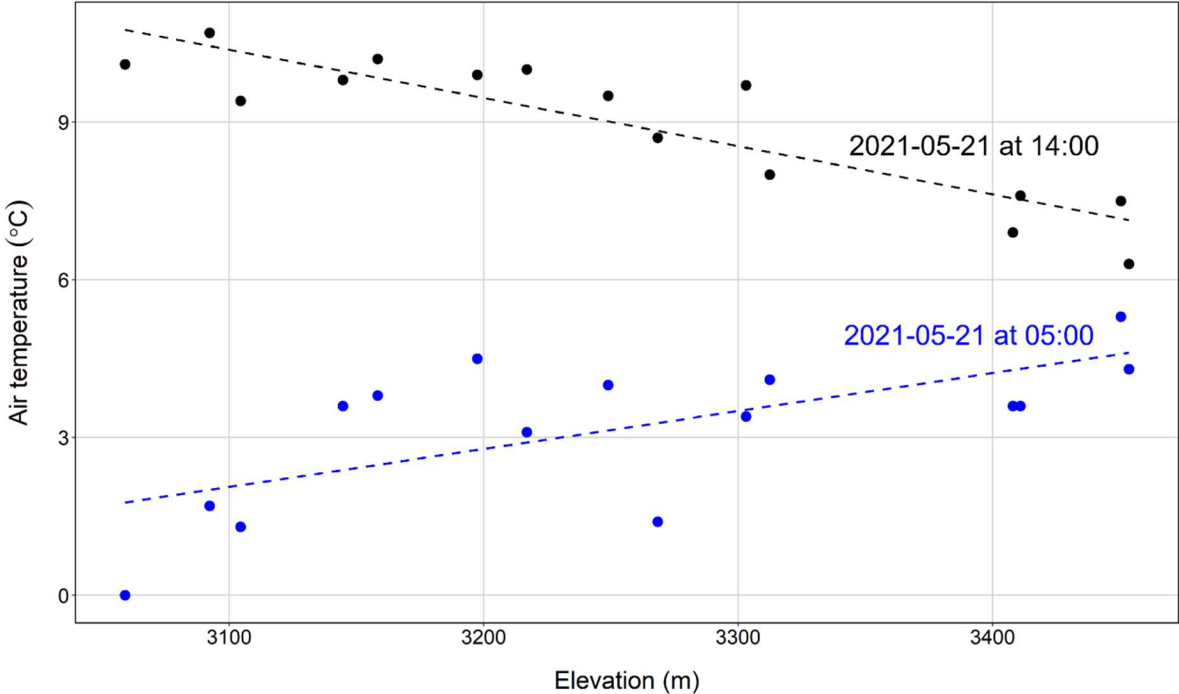


Figure 2-4. Air temperature over an elevation gradient on May 21, 2021 at 05:00 and 14:00.

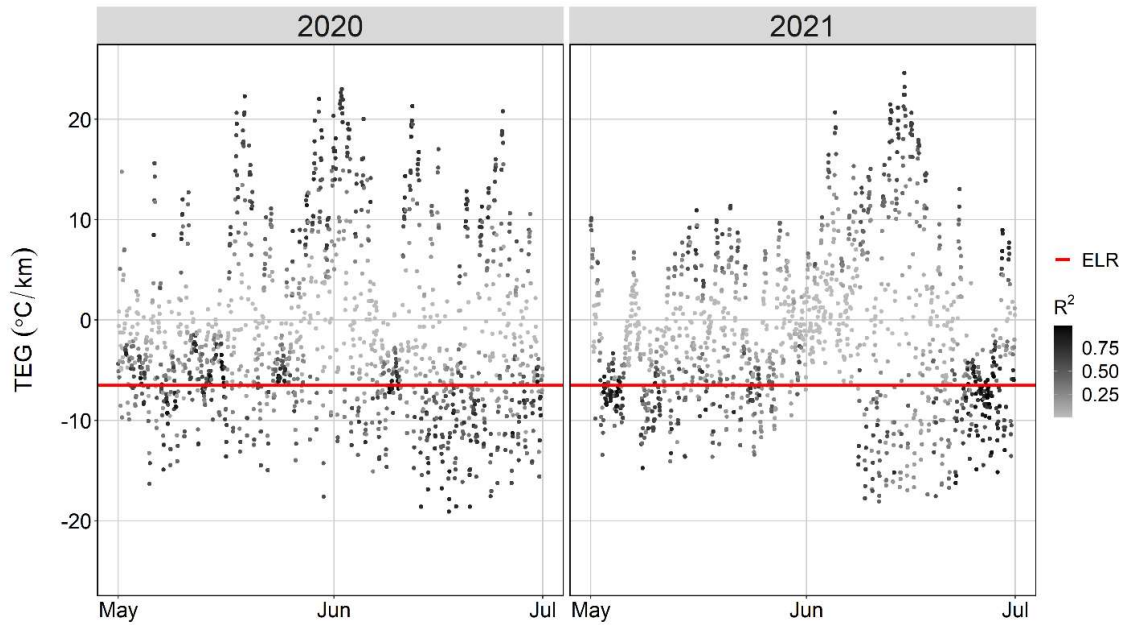


Figure 2-5. Hourly TEG values for the 2020 and 2021 snowmelt seasons. The shading of the points represents the  $R^2$  value with lighter colors being less of a correlation between air temperature and elevation. The red line represents the ELR ( $-6.5\text{ }^{\circ}\text{C}/\text{km}$ ).

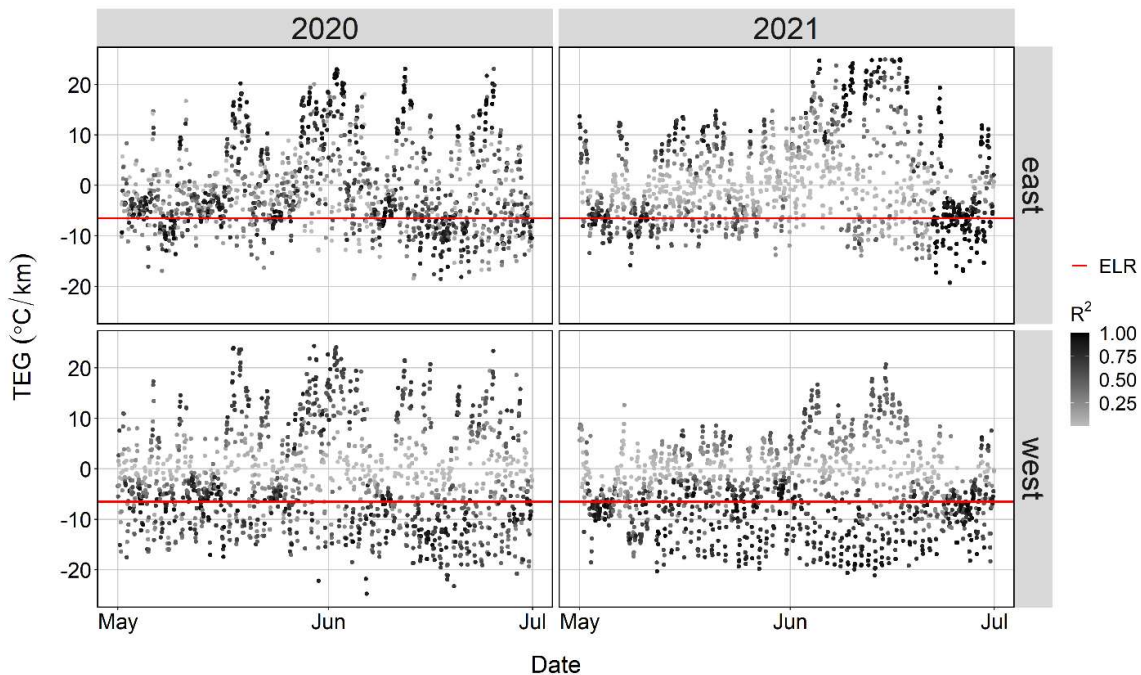


Figure 2-6. TEG values for the 2020 and 2021 snowmelt seasons separated by transect. The east transect is represented in the top graphs and the west in the bottom graphs. The shading of the points represents the  $R^2$  value with lighter colors being less of a correlation between air temperature and elevation. The red line represents the ELR.

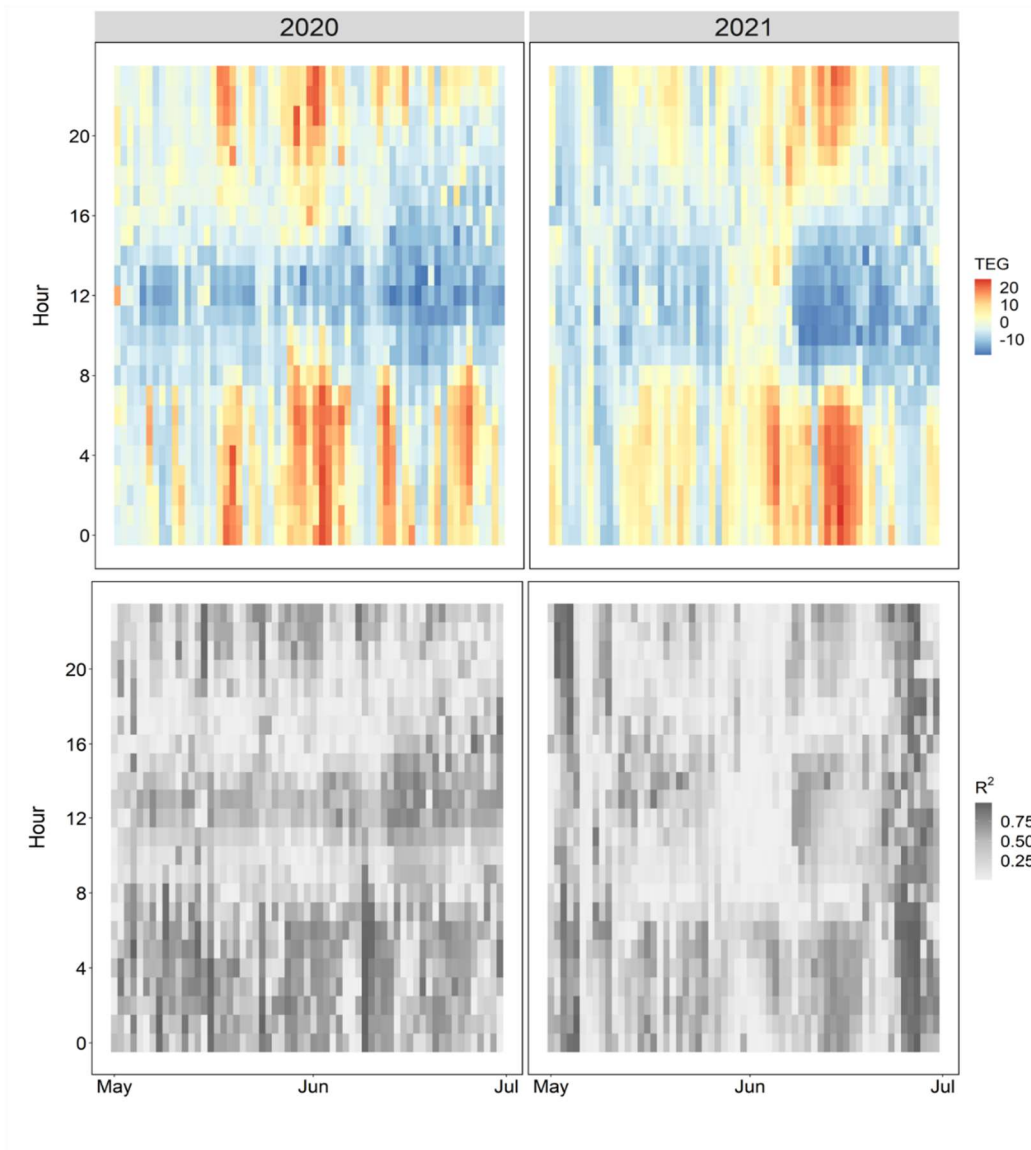


Figure 2-7. TEG (top) and  $R^2$  values (bottom) based on date and time of day. Positive TEG values are represented in yellow to red and negative in blue.  $R^2$  values are represented on a grayscale with darker representing a stronger correlation between air temperature and elevation.

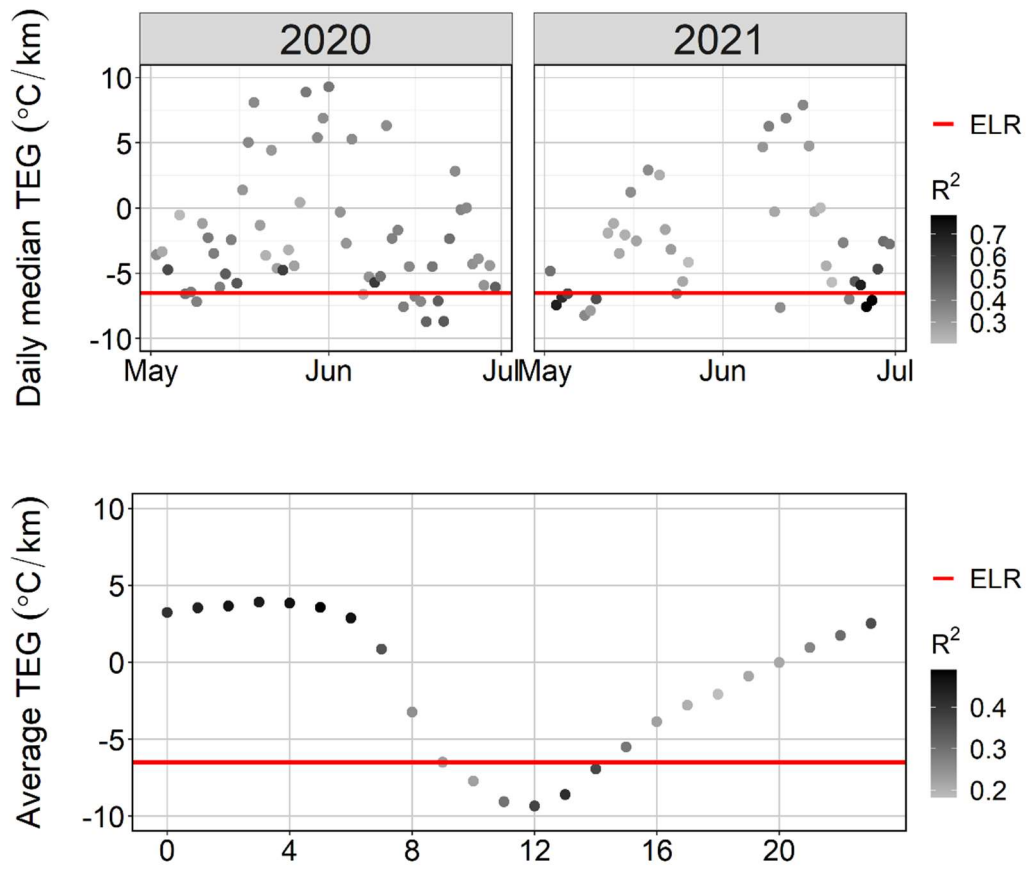


Figure 2-8. Daily median TEG computed from hourly TEG for May through June 2020 and 2021 (top) and average hourly TEG for May and June 2020 and 2021 (bottom). Daily TEG values with poor correlations (less than  $0.2 R^2$ ) were not included. The red line represents the ELR in all plots.

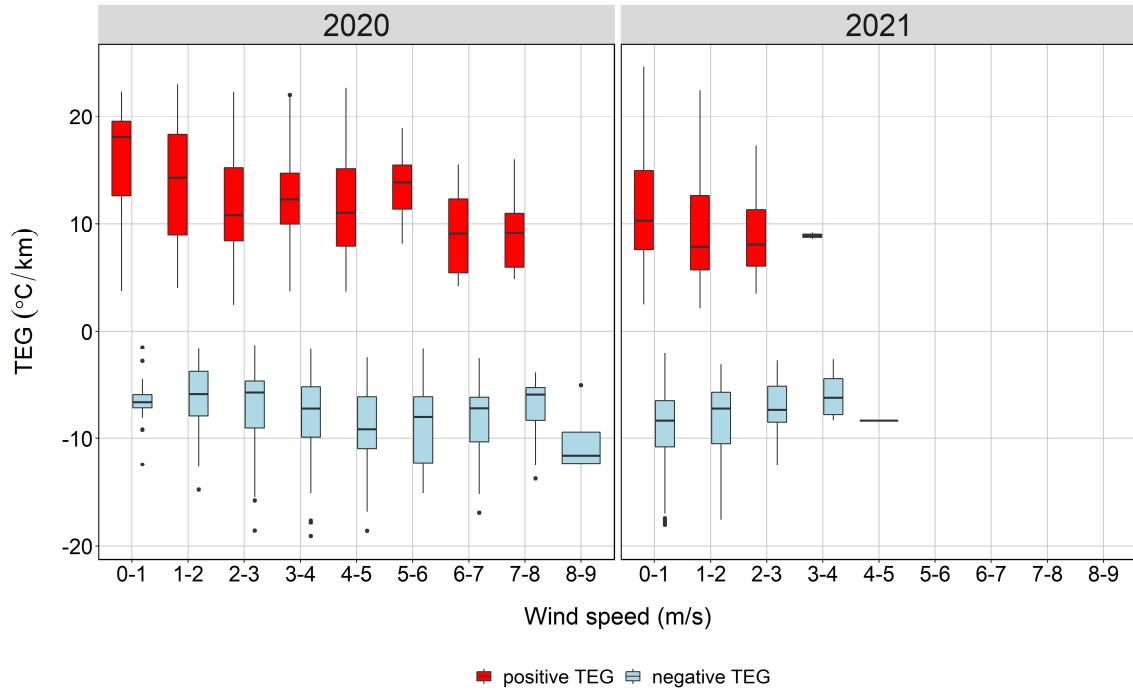


Figure 2-9. Wind speed compared to positive (top) and negative (bottom) TEG for 2020 and 2021.

Table 2-2. Average TEG, DTEG, and  $R^2$  values isolated by year, transect, or both.

Variable	Year	Transect	Average TEG or DTEG (standard deviation)	Average $R^2$ (standard deviation)
TEG	2020-21	East and west	-1.50 ( $\pm 8.11$ )	0.33 ( $\pm 0.27$ )
TEG	2020	East and west	-1.44 ( $\pm 8.45$ )	0.36 ( $\pm 0.26$ )
TEG	2021	East and west	-1.55 ( $\pm 7.75$ )	0.30 ( $\pm 0.27$ )
TEG	2020-21	East	-0.04 ( $\pm 8.97$ )	0.45 ( $\pm 0.34$ )
TEG	2020-21	West	-2.85 ( $\pm 8.95$ )	0.46 ( $\pm 0.30$ )
TEG	2020	East	-0.95 ( $\pm 8.46$ )	0.50 ( $\pm 0.32$ )
TEG	2020	West	-1.78 ( $\pm 9.89$ )	0.44 ( $\pm 0.29$ )
TEG	2021	East	0.86 ( $\pm 9.37$ )	0.40 ( $\pm 0.35$ )
TEG	2021	West	-3.93 ( $\pm 7.77$ )	0.47 ( $\pm 0.31$ )
DTEG	2020-21	East and west	-6.26 ( $\pm 9.17$ )	0.27 ( $\pm 0.29$ )
DTEG	2020	East and west	-5.70 ( $\pm 4.62$ )	0.39 ( $\pm 0.24$ )
DTEG	2021	East and west	-6.80 ( $\pm 12.10$ )	0.15 ( $\pm 0.17$ )
DTEG	2020-21	East	-6.77 ( $\pm 10.94$ )	0.45 ( $\pm 0.28$ )
DTEG	2020-21	West	-5.78 ( $\pm 1.46$ )	0.29 ( $\pm 0.27$ )
DTEG	2020	East	-6.58 ( $\pm 4.88$ )	0.52 ( $\pm 0.25$ )
DTEG	2020	West	-4.75 ( $\pm 5.52$ )	0.42 ( $\pm 0.29$ )
DTEG	2021	East	-6.95 ( $\pm 14.68$ )	0.37 ( $\pm 0.29$ )
DTEG	2021	West	-6.82 ( $\pm 13.64$ )	0.16 ( $\pm 0.17$ )

Table 2-3. Average TEG and R<sup>2</sup> values isolated by year and time of day for May through June 2020 and 2021. Daytime values represent 08:00 to 18:00 and nighttime values 17:00 to 07:00.

<b>Year and time step</b>	<b>Average TEG and standard deviation</b>	<b>R<sup>2</sup> average and standard deviation</b>
Full day 2020 and 2021	-1.50 (±8.11)	0.33 (±0.27)
Full day 2020	-1.44 (±8.44)	0.36 (±0.26)
Full day 2021	-1.55 (±7.75)	0.30 (±0.27)
Daytime 2020 and 2021	-5.97 (±5.52)	0.28 (±0.24)
Daytime 2020	-6.15 (±5.69)	0.30 (±0.23)
Daytime 2021	-5.78 (±5.35)	0.26 (±0.25)
Nighttime 2020 and 2021	2.29 (±8.01)	0.38 (±0.28)
Nighttime 2020	2.55 (±8.34)	0.41 (±0.28)
Nighttime 2021	2.03 (±7.67)	0.34 (±0.28)

#### 2.4.2 Observed dew point temperature and DTEG

Dew point temperature elevation gradients (DTEG) were quantified as a surrogate for vapor pressure gradients, since the two are directly related. The DTEG generally ranged between -20 to 10 °C/km (Figure 2-10 and Figure 2-11). This range is smaller than observed for TEG (Figures Figure 2-5 and Figure 2-6). For 2020 and 2021, the dew point temperature was poorly correlated, i.e., low R<sup>2</sup> values, when DTEG was small, i.e., approaching 0 °C/km. Positive DTEG had stronger correlations for values of 5 to 10 °C/km. Conversely, for negative DTEG, the strongest correlations were observed from -5 to -20 °C/km (Figure 2-10), which are in the range of the Kunkel (1989) DTEG. The DTEG correlations were poorer in 2021 compared to 2020 (Figure 2-10), especially for the west transect in 2021, which also had the largest range (Figure 2-11). The average DTEG parsed by transect, year, or a combination ranged between -6.95 to -4.75 °C/km with R<sup>2</sup> values ranging from 0.17 to 0.29 (Table 2-2). As shown in Figure 2-12, more positive DTEG values are generally observed during nighttime or early morning hours with variable R<sup>2</sup> values.

Unlike TEG, daily median DTEG were not parsed based on a  $R^2$  value of 0.2 since in 2021 that only includes 13% percent of the data. The difference between daily TEG correlation in 2020 and 2021 was notable (Figure 2-13). In 2021, four BM sensors were installed in the alpine. To understand if the new BM sensors were influencing the poor correlation, the DTEG values were recomputed for 2021 without the new alpine BM sensors. The average  $R^2$  for daily DTEG increases when the four alpine BM sensors are removed (0.29 to 0.36) and a total of 30 percent of the DTEG values have a  $R^2$  greater than 0.2 (Figure 2-13). Even with the four alpine BM sensors removed, there are poor correlations in May and early June.

Even more so than TEG, during higher winds, positive DTEG values were not observed (Figure 2-14). However, positive DTEG occurred 6 percent of the time. Dividing the dataset by wind speed bin (Figure 2-14), the average DTEG ranges from -6.73 to -5.72 °C/km. When considering only positive DTEG, the mean ranged from 4.68 to 7.91 °C/km (Figure 2-14). Overall, positive DTEG values did not occur when wind speeds were high.

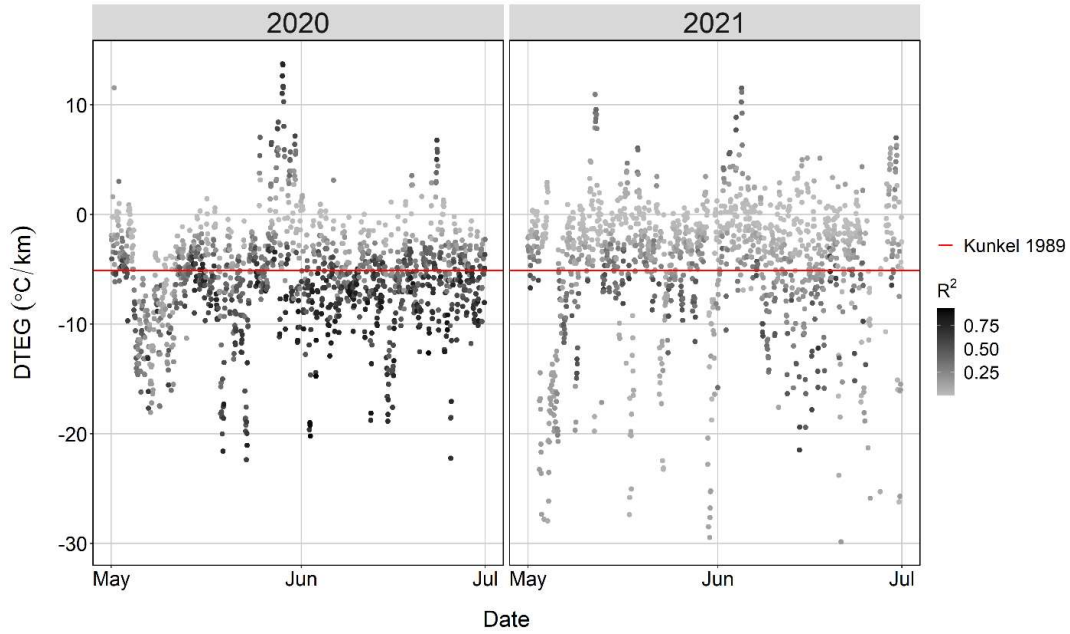


Figure 2-10. DTEG values for the 2020 and 2021 snowmelt seasons. The shading of the points represents the  $R^2$  value with lighter colors being less of a correlation between dew point temperature and elevation. The red line represents the Kunkel (1989) dew point temperature lapse rate ( $-5.1\text{ }^{\circ}\text{C}/\text{km}$ ).

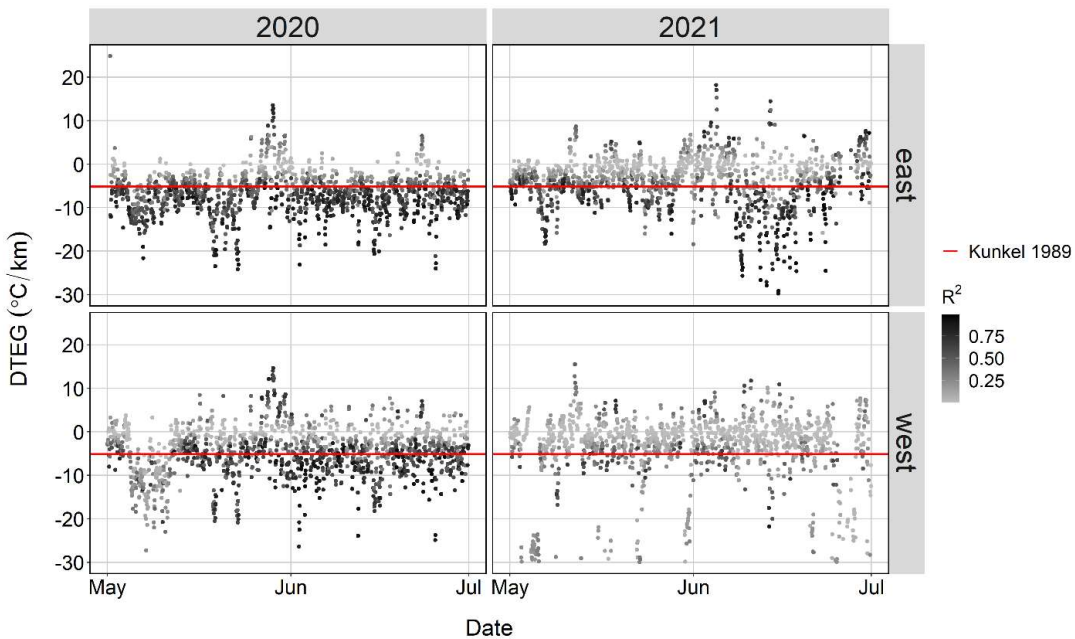


Figure 2-11. DTEG values for the 2020 and 2021 snowmelt seasons separated by transect. The east transect is represented in the top graphs and the west in the bottom graphs. The shading of the points represents the  $R^2$  value with lighter colors being less of a correlation between dew point temperature and elevation. The red line represents the Kunkel (1989) dew point temperature lapse rate.

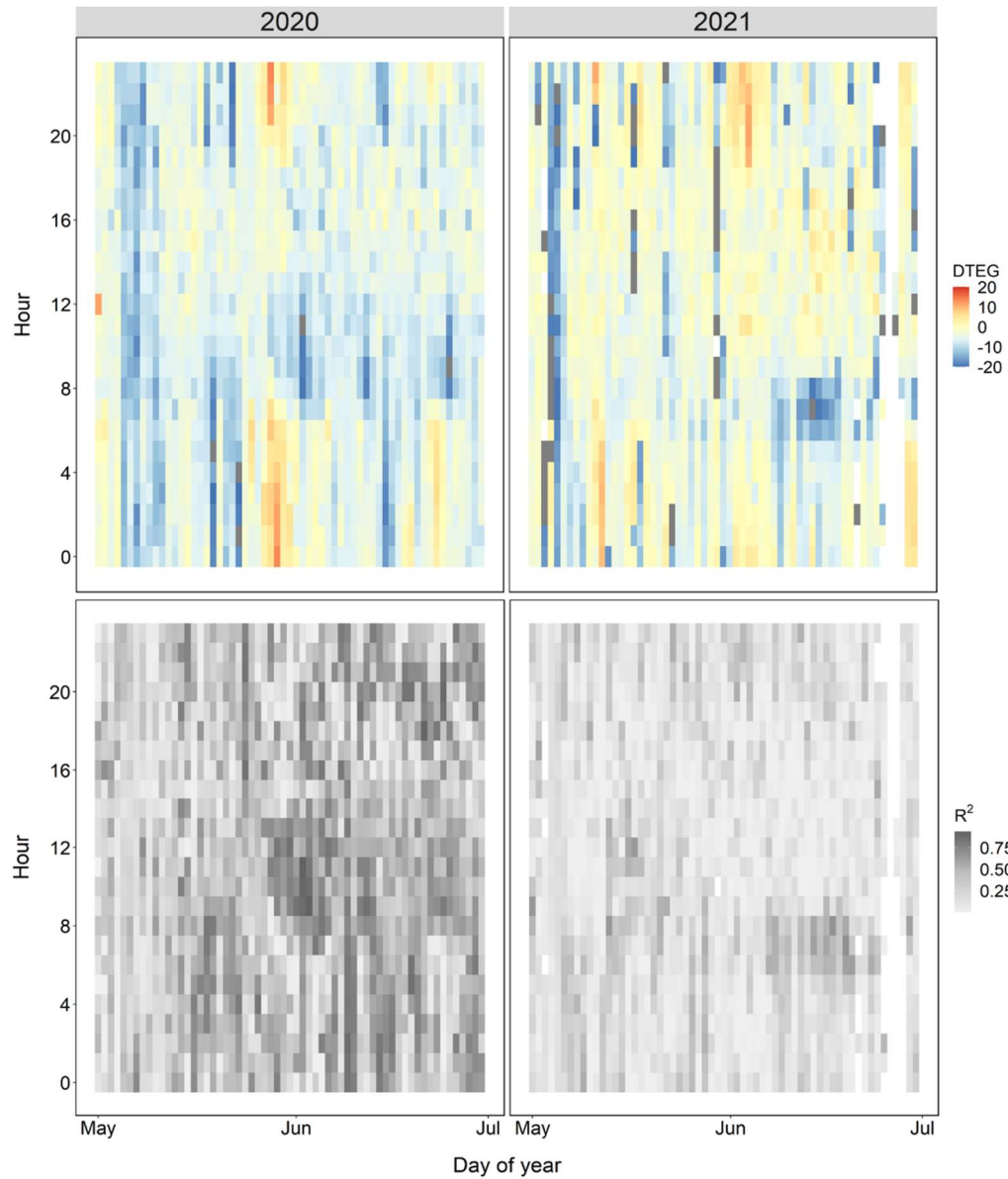


Figure 2-12. DTEG (top) and  $R^2$  values (bottom) based on date and time of day. Positive TEG values are represented in orange to red and negative in yellow to blue.  $R^2$  values are represented on a grayscale with darker representing a stronger correlation between dew point temperature and elevation.

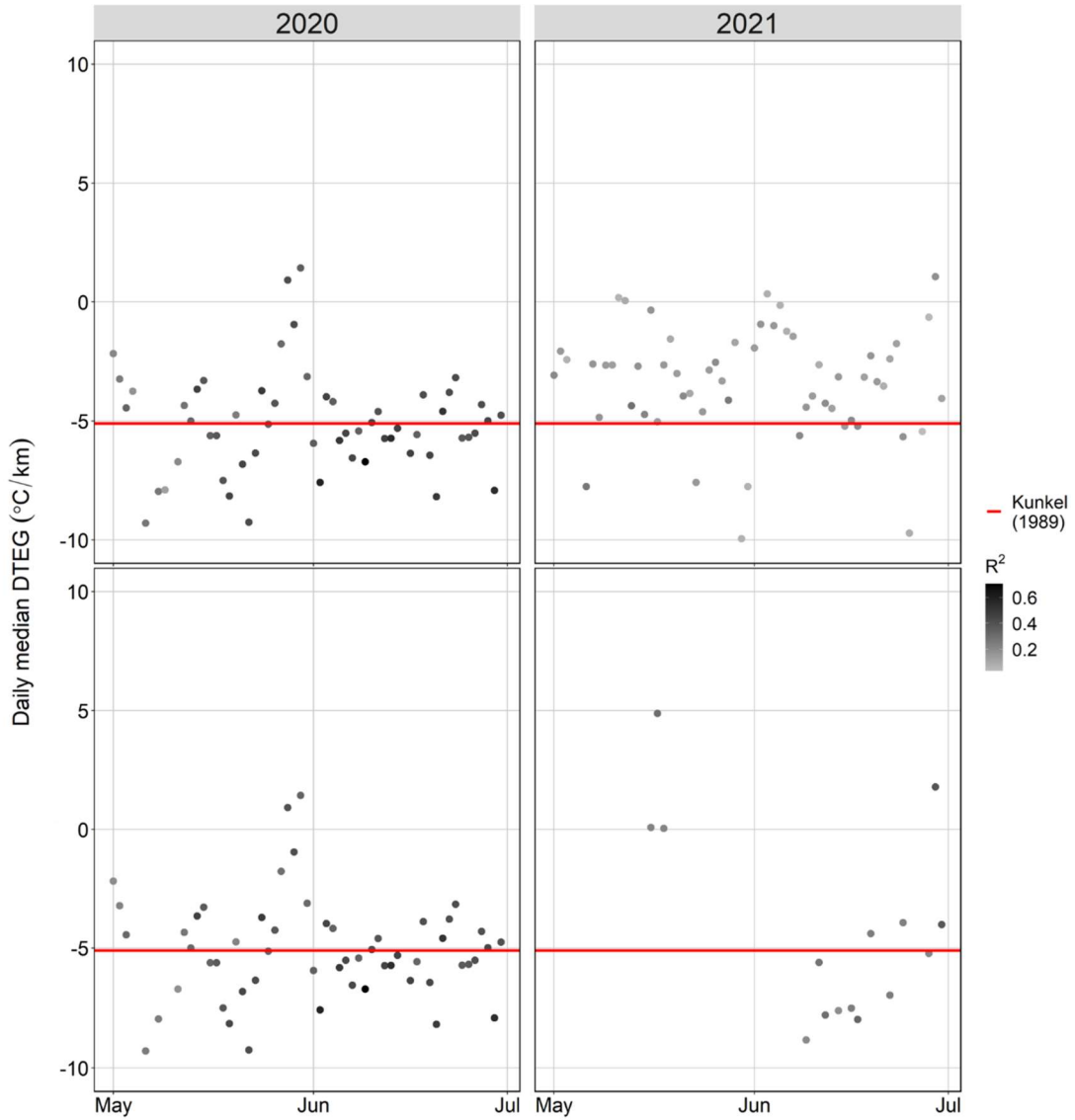


Figure 2-13. Daily median DTEG for May through June for 2020 and 2021 (top) and daily median DTEG for May through June 2020 and 2021 where  $R^2$  less than 0.2 and four alpine BM sensors are not included (bottom). The red line represents the Kunkel (1989).

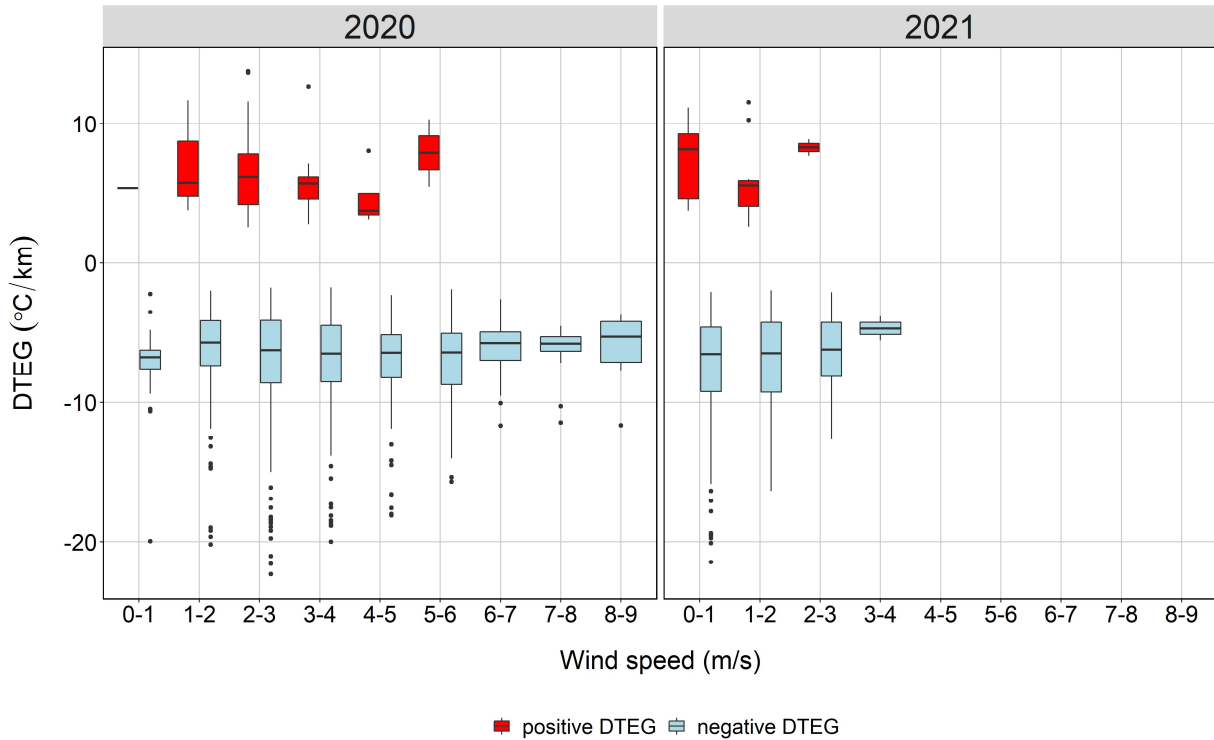


Figure 2-14. Wind speed compared to positive (bottom) and negative (top) DTEG for 2020 and 2021.

### 2.4.3 Snowmelt modeling

All scenarios (Table 2-1) produce similar snowmelt results (Figure 2-15). Scenarios ELR T, local lapse T, and local lapse T &  $T_d$  have the latest SAG dates (June 24, June 25, and June 24, respectively; Table 2-4). Model scenario obs T & lapse  $T_d$  was most similar to the base case (model scenario obs T; Figure 2-15). Model scenario obs T, the base case, best fit the observed SWE. On May 12, the observed SWE was 693 mm, and the base case was only 2% less at 680 mm, while on May 27, they were the same at 606 mm. On the last SWE observation on June 10, the model base case SWE (293 mm) was 29% greater than observed (220 mm).

Using only the temperature index approach (scenarios obs T & simpler model and local lapse T & simpler model) overestimated SWE for the first part of the snowmelt season (Figure 2-15). However, model scenario obs T & simpler model, performs well toward the end of

snowmelt season with a one-day difference in SAG date compared to the base case, scenario obs T (Table 2-4). The largest SAG difference was 6 days later from model scenario local lapse T compared to the base case (Table 2-4). Overall, the temperature and radiation index model and temperature index model performed well compared to observed SWE.

To better understand the implications, cumulative melt from model scenario obs T was used as the base case, and each treatment scenario were compared to it (Figure 2-16). As shown in Figure 2-16, model scenario ELR T performs better than model scenario local lapse T when compared to observed values. Model scenarios obs T & local lapse  $T_d$  and obs T & simpler model both use observed air temperatures and outperform all treatment scenarios. Model scenario obs T & simpler model uses the temperature index snowmelt model, whereas model scenario obs T & lapse  $T_d$  uses the temperature and radiation index model. Model scenarios local lapse T and local lapse T & simpler model had the largest RMSE and both used the Liston and Elder (2006) TEG. Model scenario local lapse T &  $T_d$ , which uses the Liston and Elder (2006) TEG, followed after model scenarios local lapse T and local lapse T & simpler model suggest this TEG is not representative of JWC.

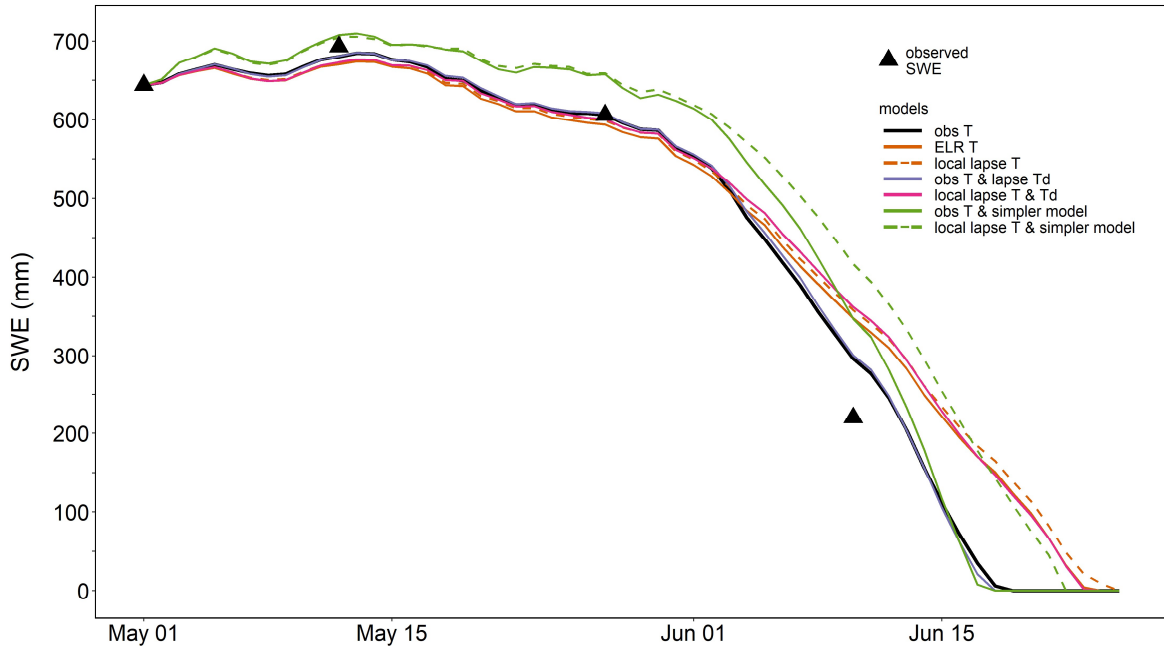


Figure 2-15. Snowmelt modeling using varying air temperature and vapor pressure gradients beginning on May 1<sup>st</sup>, 2021 to SAG for each scenario. The triangles represent observed SWE values.

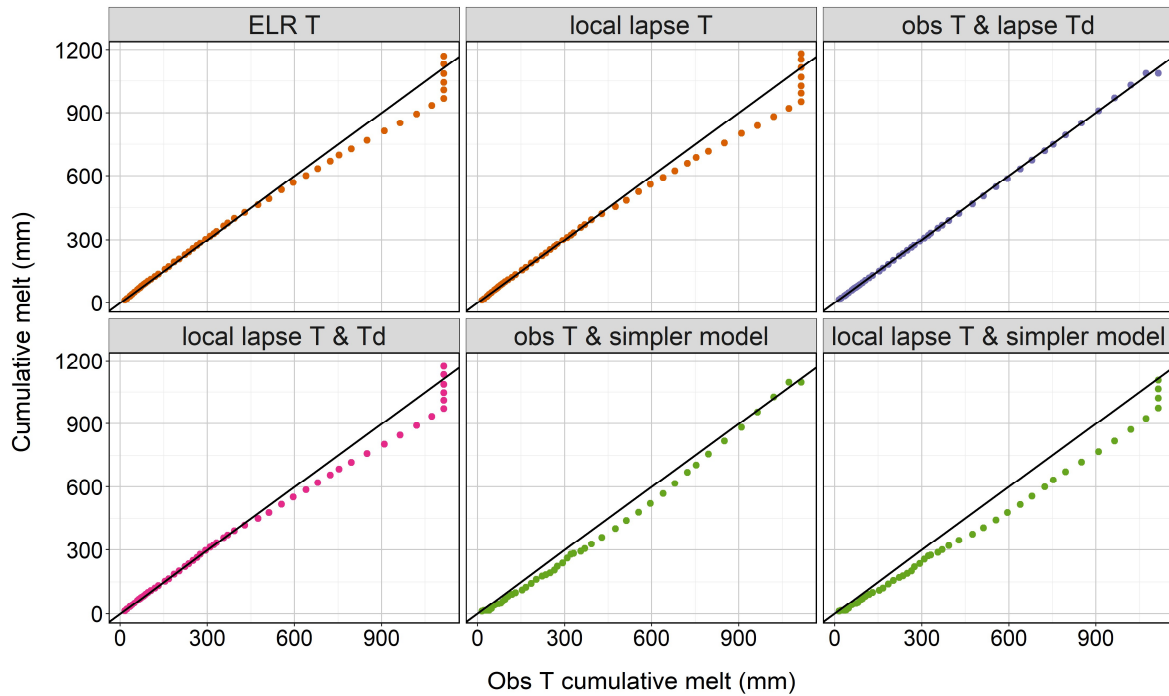


Figure 2-16. A comparison of cumulative melt for model obs T (control) and all treatment scenarios. The black line represents the 1:1.

Table 2-4. SAG date for each snowmelt model scenario

<b>Model</b>	<b>2021 SAG date</b>
obs T	June 19
ELR T	June 24
local lapse T	June 25
obs T & lapse T <sub>d</sub>	June 18
local lapse T & T <sub>d</sub>	June 24
obs T & simpler model	June 18
local lapse T & simpler model	June 22

## 2.5 Discussion

### 2.5.1 Observed air temperature and TEG

In this study, we found that hourly TEG are highly variable (Figure 2-5, Figure 2-6, and Figure 2-7) and often are not similar to the ELR or Liston and Elder (2006) TEG. The ELR is more similar to a wet adiabatic lapse rate and the Liston and Elder (2006) TEG is more similar to a dry adiabatic lapse rate. The dry adiabatic lapse rate assumes the parcel of air is dry and a wet adiabatic lapse rate assumes as the air parcel rises, water condenses and produces heat, which warms air around it (Dingman, 2002). In May 2021, hourly TEG ranges less than May 2020 (Figure 2-10). The onset of melt in 2021 did not begin until mid- to late-May, whereas in 2020 melt started prior to May 1. In May 2021, the snowpack was still accumulating until mid to late-May. This could influence the TEG correlation. Since there is high variability in hourly TEG, the daily median TEG was also computed (Figure 2-8). The nighttime positive values are inversions or cold air drainage, as seen in late summer by Collados-Lara et al. (2021). Inversions are often from downslope winds moving from high elevations (i.e., katabatic winds) influenced by the higher density of cold air (Clements et al., 2003). Several studies have encountered nightly cold air drainage (Collados-Lara et al., 2021; Follum et al., 2015; Lundquist and Cayan, 2007; Navarro-Serrano et al., 2018; Rolland, 2003). On a hillslope scale, Collados-Lara et al. (2021) found the inversions to be up to 250 °C/km, which is an order of magnitude greater than TEG

found in this study. On a macroscale, Navarro-Serrano et al. (2018) found inversions to have up to  $-5$  °C/km TEG value. Other influences on inversions can include daytime shortwave radiation, where there is greater heating at higher elevations (Kattel et al., 2015); this was not evaluated in this study since net shortwave radiation was assumed to be constant across the study domain.

The temperature inversions generally occurred during the night and into the early morning hours, indicating a diurnal pattern. This can occur diurnally based on synoptic meteorological conditions, which includes negative net radiation (i.e., low solar radiation), clear conditions, high atmospheric pressure, and light winds. During these conditions, the net radiation and the surface begins to cool (i.e., radiation cooling). Since cooler air is denser, it begins to drain downslope and is replaced by warmer air above, which causes the inversion (Daly et al., 2009). When there are higher wind speeds, these layers (cold and warm) mix and inversions are not observed. Since cold air drainage can be associated with calm nights (i.e., low wind speeds), this study considered wind speed and whether there was a relationship between positive or negative TEG (Figure 2-9), similar to Clements et al. (2003) and Collados-Lara et al. (2021). When higher wind speeds occurred, there were negative TEG values, thus a relationship between wind speed and TEG exists. However, the anemometer used for this study was located 3.2 km south of the study domain and located on an east aspect. Only 5 of the 18 BM sensors are located on an east aspect. A comparison between wind direction and positive and negative TEG were evaluated and no significant relationship was identified. An analysis similar to the automated algorithm for cold air drainage or pooling explained in Lundquist et al. (2008) prior to using the ELR or published TEG values could provide insight. The automated algorithm uses DEMs to analyze slope, aspect, curvature, and percentile elevation relative to surrounding terrain to see if

the air is draining or pooling (Lundquist et al., 2008). If cold air drainage is found within the study domain, using different nighttime and daytime TEG could provide better accuracy.

### *2.5.2 Observed dew point temperature and DTEG*

In this study, hourly DTEG values were compared to the Kunkel (1989) value of  $-5.1$  °C/km (Figure 2-10, Figure 2-11, and Figure 2-12). Similar to TEG (Figure 2-5, Figure 2-6, and Figure 2-7), there is high variability in hourly values, thus daily values were also evaluated (Figure 2-13). Overall, daily and hourly DTEG were less variable than TEG and behaved more similarly to published values. Another difference between the TEG and DTEG behavior is that there was a stronger relationship between wind speed and DTEG (Figure 2-9 and Figure 2-14).

The average hourly DTEG of  $-1.5$  °C/km (Table 2-2) is similar to the Franklin (1983) DTEG of  $-1.25$  °C/km. The Franklin (1983) DTEG used observed dew point temperatures from a watershed in north Idaho. Conversely, the average daily DTEG for May and June 2020 and 2021 was  $-5.1$  °C/km, which equals the Kunkel (1989) DTEG. Feld et al. (2013) reported that assuming linear trends for DTEG (Kunkel, 1989) is not always appropriate. However, the Feld et al. (2013) study site was in Sierra Nevada, which has a wetter climate than JWC and thus generally more atmospheric moisture.

There are stronger correlations between dew point temperature and elevation in May 2020 than 2021 (Figures Figure 2-10, Figure 2-11, Figure 2-12, and Figure 2-13). As stated in the previous section, May and June 2020 represent the full melt period, whereas in 2021, the snowpack was still accumulating in May. Therefore, there was likely more atmospheric moisture in May 2021 than May 2020 resulting in a less linear correlation between dew point temperature and elevation. Another difference between May 2020 and 2021 is there were four additional BM sensors installed to represent the alpine conditions. As shown in Figure 2-13, removing the

alpine BM sensors improved the linear dew point temperature-elevation correlation. Further investigation into the dew point temperatures in the alpine and other meteorological influences that occurred in 2021 are needed to understand the poor correlation between dew point temperature and elevation.

### 2.5.3 *Snowmelt modeling*

The SAG date for the treatment model scenarios ranged from a 1 to 6-day difference when compared to the base case (obs T), which could yield a shift in peak snowmelt runoff. Conversely, Minder et al. (2010) found snowpack shifts a month earlier when changing the lapse rate by 1.5 °C/km in the Cascade Mountains, which is a similar change between the Liston and Elder (2006) TEG and the ELR used in this study. Overall, model scenarios that used observed air temperatures (obs T & lapse  $T_d$  and obs T & simpler model) perform best (Figure 2-16 and Table 2-4). When estimating air temperatures in snowmelt modeling, the ELR provides better estimates than the Liston and Elder (2006) TEG. Due to the inversions that occur, the average is shifted and becomes less negative making the ELR more suitable. The average TEG is negative between 08:00 to 19:00 when incoming shortwave radiation is at its greatest (Figure 2-8). Consequently, a large portion of snowmelt occurs during those hours making the ELR suitable regardless of the strong inversions that occur.

In model scenarios obs T & lapse  $T_d$  and local lapse T &  $T_d$ , the DTEG was manipulated to understand the importance of vapor pressure on incoming longwave radiation and its effect on snowmelt. Model scenario obs T & lapse  $T_d$  performs almost identically to the base case (Figure 2-15). Therefore, when using the temperature and radiation index snowmelt model, the Kunkel (1989) DTEG is suitable. Model scenario local lapse T &  $T_d$  also used the Kunkel (1989) DTEG, but the model most likely performs second worst (after model scenario ELR T) since the

differences are due primarily to the use of the constant Liston and Elder (2006) TEG. Since dew point temperature is less variable than air temperature, dew point temperature has little impact on snowmelt. Dew point temperature (or vapor pressure) is a function of emissivity, which is a variable in incoming longwave (Equations 2-4 and 2-5). Therefore, dew point temperature has a less direct effect on snowmelt modeling than air temperature. However, since dew point temperature can influence losses or gains due to sublimation, a model that incorporates the latent heat flux could show more sensitivity to dew point temperature (Feld et al., 2013). Our SAG results (Table 2-4) when manipulating DTEG were similar to Feld et al. (2013) in that there was a difference of a few days between observed and estimated.

This study found that the complexity of the snowmelt index model used (equation 2-2 versus 2-3) is not as important for model performance as using observed air temperature. While model scenarios obs T & simpler model and local lapse T & simpler model (both temperature index model), underpredict in the beginning of the season, the SAG dates are satisfactory when compared to the base case (June 18 and June 22, respectively; Table 2-4 and Figure 2-13 and Figure 2-14). Since variable melt factors are used in the temperature index model it accounts for increases of net shortwave radiation as the melt season progresses (Fassnacht et al., 2017). Although the temperature index snowmelt model is simple, it can be an adequate alternative in JWC or similar regimes when net radiation data are not available (Hock, 2003; Ohmura, 2001). Conversely, Follum et al. (2019) found that in Senator Beck Basin, Colorado, adding radiation to the temperature index model improved performance.

Since net radiation was not measured at the point snowmelt modeling location, several components were estimated. Due to issues with the measured shortwave radiation, it was estimated using daily albedo; this has been shown to be less accurate than a variable daily albedo

(Reimanis, 2021). Additionally, incoming shortwave radiation and outgoing longwave radiation were assumed to be similar between the modeling point location and the CAIC weather station, as per Follum et al. (2015). From the performance of the snowmelt model scenarios on May 12 and 27 compared to observed SWE (Figure 2-16), the estimations were sufficient. There is a notable difference (29.5 percent difference) from observed SWE for model scenario obs T (base case) on June 10. This large difference could be based on the melt factors being calibrated from the Joe Wright SNOTEL. At Joe Wright SNOTEL, SAG occurred on June 11, whereas at the snowmelt modeling location (point SWE-17 in Figure 2-1), there was still more than 200 mm of SWE. Therefore, the melt factors may not account for the conditions that occurred after June 11. Conversely, the daily temperature melt factors used in the temperature index snowmelt model from Fassnacht et al. (2017) were calibrated using the Lake Irene SNOTEL station, since melt factor data were missing for several semi-monthly periods at the Joe Wright SNOTEL. Therefore, it seems the melt factors are more sensitive to manipulation in the temperature and radiation index snowmelt model. Future work should include more observed snow surveys throughout the season or SCA data to better understand the performance of the model, and calibrating melt factors (if using the temperature and radiation index snowmelt model) at a similar elevation or location where the model is being utilized.

## **2.6 Conclusions**

We found the hourly TEG and DTEG values to be variable temporally. The average hourly TEG value was  $-1.50\text{ }^{\circ}\text{C}/\text{km}$  ( $\pm 8.11$ ). Positive TEG values generally occurred at nighttime and negative values during daytime. The ELR is applicable during the daytime for this study domain. However, further investigation should be done prior to applying ELR at nighttime in similar regimes (e.g., cold air drainage mapping, installing temperature sensors). A

relationship between wind speed and positive or negative TEG and DTEG values were observed; higher wind speeds correlated with negative TEG and DTEG values. The hourly DTEG value was  $-6.26\text{ }^{\circ}\text{C}/\text{km}$  ( $\pm 9.17$ ), and was less variable than TEG. The DTEG had poor correlations when alpine BM sensors were included. Therefore, further exploration to understand dew point fluctuations in the alpine is necessary.

The ELR resulted in more accurate snowmelt modeling results than the Liston and Elder (2006) TEG. Although the ELR performed better than the Liston and Elder (2006) TEG, the model scenario incorporating ELR had a later SAG date by 5 days. The Kunkel (1989) DTEG performed similarly to observed dew point temperatures and the temperature and radiation index model was not sensitive to this manipulation. The temperature index model is a satisfactory snowmelt model to utilize when limited meteorological values are available. Additionally, the temperature and radiation index model can be utilized with limited meteorological variables if net radiation is estimated similar to the procedures used in this study.

## 2.7 References

- Barry, R., & Chorley, R. (1987). *Atmosphere, Weather, and Climate* (1<sup>st</sup> ed.). Associated Book Publishers.
- Blandford, T. R., Humes, K. S., Harshburger, B. J., Moore, B. C., Walden, V. P., & Ye, H. (2008). Seasonal and synoptic variations in near-surface air temperature lapse rates in a mountainous basin. *Journal of Applied Meteorology and Climatology*, *47*(1), 249–261. <https://doi.org/10.1175/2007JAMC1565.1>
- Blöschl, G. (1999). Scaling issues in snow hydrology. *Hydrological Processes*, *13*(14–15), 2149–2175. [https://doi.org/10.1002/\(SICI\)1099-1085\(199910\)13:14/15<2149::AID-HYP847>3.0.CO;2-8](https://doi.org/10.1002/(SICI)1099-1085(199910)13:14/15<2149::AID-HYP847>3.0.CO;2-8)
- Brubaker, K., Rango, A., & Kustas, W. (1996). Incorporating radiation inputs into the snowmelt runoff model. *Hydrological Processes*, *10*(10), 1329–1343. [https://doi.org/10.1002/\(sici\)1099-1085\(199610\)10:10<1329::aid-hyp464>3.0.co;2-w](https://doi.org/10.1002/(sici)1099-1085(199610)10:10<1329::aid-hyp464>3.0.co;2-w)
- Cazorzi, F., & Dalla Fontana, G. (1996). Snowmelt modelling by combining air temperature and a distributed radiation index. *Journal of Hydrology*, *181*(1–4), 169–187. [https://doi.org/10.1016/0022-1694\(95\)02913-3](https://doi.org/10.1016/0022-1694(95)02913-3)

- Clements, C. B., David Whiteman, C., & Horel, J. D. (2003). Cold-air-pool structure and evolution in a mountain basin: Peter Sinks, Utah. *Journal of Applied Meteorology*, 42(6), 752–768. [https://doi.org/10.1175/1520-0450\(2003\)042<0752:CSAEIA>2.0.CO;2](https://doi.org/10.1175/1520-0450(2003)042<0752:CSAEIA>2.0.CO;2)
- Collados-Lara, A. J., Fassnacht, S. R., Pulido-Velazquez, D., Pfohl, A. K. D., Morán-Tejeda, E., Venable, N. B. H., Pardo-Igúzquiza, E., & Puntenney-Desmond, K. (2021). Intra-day variability of temperature and its near-surface gradient with elevation over mountainous terrain: Comparing MODIS land surface temperature data with coarse and fine scale near-surface measurements. *International Journal of Climatology*, 41, E1435–E1449. <https://doi.org/10.1002/joc.6778>
- Daly C., Conklin, D.R., Unsworth, M.H. (2009). Local atmospheric decoupling in complex topography alters climate change impacts. *International Journal of Climatology*, 30(12), 1857-1864. <https://doi.org/10.1002/joc.2007>
- Dingman, L. S. (2015). *Physical Hydrology* (I. Waveland Press (ed.); Third).
- Dunn, S. M., & Colohan, R. J. E. (1999). Developing the snow component of a distributed hydrological model: A step-wise approach based on multi-objective analysis. *Journal of Hydrology*, 223(1–2), 1–16. [https://doi.org/10.1016/S0022-1694\(99\)00095-5](https://doi.org/10.1016/S0022-1694(99)00095-5)
- Fassnacht, S. R., López-Moreno, J. I., Ma, C., Weber, A. N., Pfohl, A. K. D., Kampf, S. K., & Kappas, M. (n.d.). *Spatio-temporal snowmelt variability across the headwaters of the Southern Rocky Mountains*. <https://doi.org/10.1007/s11707-017-0641-4>
- Fassnacht, S. R., López-Moreno, J. I., Ma, C., Weber, A. N., Pfohl, A. K. D., Kampf, S. K., & Kappas, M. (2017). Spatio-temporal snowmelt variability across the headwaters of the Southern Rocky Mountains. *Frontiers in Earth Science*, 11(3), 505–514. <https://doi.org/10.1007/s11707-017-0641-4>
- Fassnacht, S. R., Snelgrove, K. R., & Soulis, E. D. (2001). Daytime long-wave radiation approximation for physical hydrological modelling of snowmelt: A case study of Southwestern Ontario. *IAHS-AISH Publication*, 270, 279–286.
- Feld, S. I., Cristea, N. C., & Lundquist, J. D. (2013). Representing atmospheric moisture content along mountain slopes: Examination using distributed sensors in the Sierra Nevada, California. *Water Resources Research*, 49(7), 4424–4441. <https://doi.org/10.1002/wrcr.20318>
- Flerchinger, G. N., Xaio, W., Marks, D., Sauer, T. J., & Yu, Q. (2009). Comparison of algorithms for incoming atmospheric long-wave radiation. *Water Resources Research*, 45, 1–14. <https://doi.org/10.1029/2008WR007394>
- Follum, M. L., Downer, C. W., Niemann, J. D., Roylance, S. M., & Vuyovich, C. M. (2015). A radiation-derived temperature-index snow routine for the GSSHA hydrologic model. *Journal of Hydrology*, 529(P3), 723–736. <https://doi.org/10.1016/j.jhydrol.2015.08.044>
- Follum, M. L., Niemann, J. D., & Fassnacht, S. R. (2019). A comparison of snowmelt-derived streamflow from temperature-index and modified-temperature-index snow models. *Hydrological Processes*, 33(23), 3030–3045. <https://doi.org/10.1002/hyp.13545>
- Garcia, E. S., Tague, C. L., & Choate, J. S. (2013). Influence of spatial temperature estimation

- method in ecohydrologic modeling in the Western Oregon Cascades. *Water Resources Research*, 49(3), 1611–1624. <https://doi.org/10.1002/wrcr.20140>
- Gardner, A. S., & Sharp, M. (2009). Sensitivity of net mass-balance estimates to near-surface temperature lapse rates when employing the degree-day method to estimate glacier melt. *Annals of Glaciology*, 50(50), 80–86.
- Hamlin, L., Pietroniro, A., Prowse, T., Soulis, R., & Kouwen, N. (1998). Application of indexed snowmelt algorithms in a northern wetland regime. *Hydrological Processes*, 12(10–11), 1641–1657. [https://doi.org/10.1002/\(SICI\)1099-1085\(199808/09\)12:10/11<1641::AID-HYP686>3.0.CO;2-W](https://doi.org/10.1002/(SICI)1099-1085(199808/09)12:10/11<1641::AID-HYP686>3.0.CO;2-W)
- Harlow, R. C., Burke, E. J., Scott, R. L., Shuttleworth, W. J., Brown, C. M., & Petti, J. R. (2004). Derivation of temperature lapse rates in semi-arid south-eastern Arizona Research Note: Derivation of temperature lapse rates in semi-arid south-eastern Arizona. *Hydrology and Earth System Sciences*, 8(6), 1179–1185. <http://edcdaac.usgs.gov/>
- Hock, R. (1999). Including Potential Direct Solar Radiation. *Journal of Glaciology*, 45(149), 101–111.
- Hock, R. (2003). Temperature index melt modelling in mountain areas. *Journal of Hydrology*, 282, 104–115. [https://doi.org/10.1016/S0022-1694\(03\)00257-9](https://doi.org/10.1016/S0022-1694(03)00257-9)
- Hubbart, J. A. (2011). An Inexpensive Alternative Solar Radiation Shield for Ambient Air Temperature Micro-Sensors. *Journal of Natural & Environmental Sciences*, 2(2), 9–14.
- Immerzeel, W., Petersen, L., Ragettli, S., & Pellicciotti, F. (2014). The importance of observed gradients of air temperature and precipitation for modeling runoff from a glacierized watershed in the Nepalese Himalayas. *Water Resources Research*, 50, 2212–2226. <https://doi.org/10.1002/2013WR014506>
- Immerzeel, W. W., Petersen, L., Ragettli, S., & Pellicciotti, F. (2014). The importance of observed gradients of air temperature and precipitation for modeling runoff from a glacierized watershed in the Nepalese Himalayas. *Water Resources Research*, 50, 2212–2226. <https://doi.org/10.1002/2013WR014506>
- Kampf, S. K., & Richer, E. E. (2014). Estimating source regions for snowmelt runoff in a Rocky Mountain basin: tests of a data-based conceptual modeling approach. *Hydrological Processes*, 28, 2237–2250. <https://doi.org/10.1002/hyp.9751>
- Kattel, D. B., Yao, T., Yang, W., Gao, Y., & Tian, L. (2015). Comparison of temperature lapse rates from the northern to the southern slopes of the Himalayas. *International Journal of Climatology*, 35, 4431–4443. <https://doi.org/10.1002/joc.4297>
- Kingston, A. P., Fassnacht, S. R., & Derry, J. E. (n.d.). Fine scale data collection for future snowmelt modeling near Silverton, Colorado. *Colorado Water*.
- Kulshrestha, S., Ramsankaran, R., Kumar, A., Arora, M., & Kumar, A. (2018). Investigating the Performance of Snowmelt Runoff Model Using Temporally Varying Near-Surface Lapse Rate in Western Himalayas Estimation of rainfall using satellite Imagery with use of machine learning software WEKA View project Towards a Comprehensive Dat. *Current Science*, 114(4), 808–813. <https://doi.org/10.18520/cs/v114/i04/808-813>

- Kunkel, K. E. (1989). Simple Procedures for Extrapolation of Humidity Variables in the Mountainous Western United States. *Journal of Climate*, 2, 656–669.
- Kustas, W. P., Rango, A., & Uijlenhoet, R. (1994). A simple energy budget algorithm for the snowmelt runoff model. *Water Resources Research*, 30(5), 1515–1527. <https://doi.org/10.1029/94WR00152>
- Li, X., & Williams, M. W. (2008). Snowmelt runoff modelling in an arid mountain watershed, Tarim Basin, China. *Hydrological Processes*, 22, 3931–3940. <https://doi.org/10.1002/hyp>
- Liston, G. E., & Elder, K. (2006). A meteorological distribution system for high-resolution terrestrial modeling (MicroMet). *Journal of Hydrometeorology*, 7(2), 217–234. <https://doi.org/10.1175/JHM486.1>
- Lundquist, J. D., & Cayan, D. R. (2007). Surface temperature patterns in complex terrain: Daily variations and long-term change in the central Sierra Nevada, California. *Journal of Geophysical Research Atmospheres*, 112(11), 1–15. <https://doi.org/10.1029/2006JD007561>
- Lundquist, J. D., & Huggett, B. (2008). Evergreen trees as inexpensive radiation shields for temperature sensors. *Water Resources Research*, 46(4). <https://doi.org/10.1029/2008WR006979>
- Lundquist, J. D., Pepin, N., & Rochford, C. (2008). Automated algorithm for mapping regions of cold-air pooling in complex terrain. *Journal of Geophysical Research Atmospheres*, 113(22). <https://doi.org/10.1029/2008JD009879>
- Lute, A. C., & Abatzoglou, J. T. (2020). Best practices for estimating near-surface air temperature lapse rates. *International Journal of Climatology*, November 2019, 1–16. <https://doi.org/10.1002/joc.6668>
- Martinez, J., & Rango, A. (1986). Parameter values for snowmelt runoff modelling. *Journal of Hydrology*, 84(3–4), 197–219. [https://doi.org/10.1016/0022-1694\(86\)90123-X](https://doi.org/10.1016/0022-1694(86)90123-X)
- Minder, J. R., Mote, P. W., & Lundquist, J. D. (2010). Surface temperature lapse rates over complex terrain: Lessons from the Cascade Mountains. *Journal of Geophysical Research Atmospheres*, 115(14), 1–13. <https://doi.org/10.1029/2009JD013493>
- Misra, A., Kumar, A., Bhambri, R., Haritashya, U. K., Verma, A., Dobhal, D. P., Gupta, A. K., Gupta, G., & Upadhyay, R. (2020). Topographic and climatic influence on seasonal snow cover: Implications for the hydrology of ungauged Himalayan basins, India. *Journal of Hydrology*, 585(April 2019), 124716. <https://doi.org/10.1016/j.jhydrol.2020.124716>
- Navarro-Serrano, F., López-Moreno, J. I., Azorin-Molina, C., Alonso-González, E., Tomás-Burguera, M., Sanmiguel-Vallelado, A., Revuelto, J., & Vicente-Serrano, S. M. (2018). Estimation of near-surface air temperature lapse rates over continental Spain and its mountain areas. *International Journal of Climatology*, 38(8), 3233–3249. <https://doi.org/10.1002/joc.5497>
- Ohmura, A. (2001). Physical basis for the temperature-based melt-index method. *Journal of Applied Meteorology*, 40(4), 753–761. [https://doi.org/10.1175/1520-0450\(2001\)040<0753:PBFTTB>2.0.CO;2](https://doi.org/10.1175/1520-0450(2001)040<0753:PBFTTB>2.0.CO;2)

- Pagano, T., Garen, D., & Sorooshian, S. (2004). Evaluation of official western U.S. seasonal water supply outlooks, 1922-2002. *Journal of Hydrometeorology*, 5(5), 896–909. [https://doi.org/10.1175/1525-7541\(2004\)005<0896:EOWWUS>2.0.CO;2](https://doi.org/10.1175/1525-7541(2004)005<0896:EOWWUS>2.0.CO;2)
- Rango, A., & Martinec, J. (1996). Revisiting the Degree-Day Method for. *Water Resources Bulletin*, 31(4).
- Rangwala, I., Miller, J. R., Russell, G. L., & Xu, M. (2010). Using a global climate model to evaluate the influences of water vapor, snow cover and atmospheric aerosol on warming in the Tibetan Plateau during the twenty-first century. *Climate Dynamics*, 34, 859–872. <https://doi.org/10.1007/s00382-009-0564-1>
- Reimanis, D. C. (2021). *Variable fresh snow albedo: how snowpack and sub-nivean properties influence fresh snow reflectance*. Colorado State University.
- Richard, C., & Gratton, D. J. (2001). The importance of the air temperature variable for the snowmelt runoff modelling using the SRM. *HYDROLOGICAL PROCESSES Hydrol. Process*, 15, 3357–3370. <https://doi.org/10.1002/hyp.1031>
- Rolland, C. (2003). Spatial and seasonal variations of air temperature lapse rates in alpine regions. *Journal of Climate*, 16(7), 1032–1046. [https://doi.org/10.1175/1520-0442\(2003\)016<1032:SASVOA>2.0.CO;2](https://doi.org/10.1175/1520-0442(2003)016<1032:SASVOA>2.0.CO;2)
- Ruckstuhl, C., Philipona, R., Morland, J., & Ohmura, A. (2007). Observed relationship between surface specific humidity, integrated water vapor, and longwave downward radiation at different altitudes. *Journal of Geophysical Research Atmospheres*, 112, 1–7. <https://doi.org/10.1029/2006JD007850>
- Schneider, D., & Molotch, N. (2016). Real-time estimation of snow water equivalent in the Upper Colorado River Basin using MODIS-based SWE Reconstructions and SNOTEL data. *Water Resources Research*, 52, 7892–7910. <https://doi.org/10.1002/2016WR019067>
- Shen, Y. J., Shen, Y., Goetz, J., & Brenning, A. (2016). Spatial-temporal variation of near-surface temperature lapse rates over the Tianshan mountains, central Asia. *Journal of Geophysical Research*, 121(23), 14,006-14,017. <https://doi.org/10.1002/2016JD025711>
- Tercek, M. T., Rodman, A., Woolfolk, S., Wilson, Z., Thoma, D., & Gross, J. (2021). Correctly applying lapse rates in ecological studies: comparing temperature observations and gridded data in Yellowstone. *Ecosphere*, 12(3). <https://doi.org/10.1002/ecs2.3451>
- U.S. Army Corps of Engineers. (1956). *Snow hydrology - Summary report of the snow investigations*.
- Verseghy, D. L. (1991). Class-A Canadian land surface scheme for GCMS. I. Soil model. *International Journal of Climatology*, 11(2), 111–133.
- Wang, L., Sun, L., Shrestha, M., Li, X., Liu, W., Zhou, J., Yang, K., Lu, H., & Chen, D. (2016). Improving snow process modelign with satellite-bsaed estimation of near-surface-air temperatute lapse rate. *Journal of Geophysical Research Atmospheres*, 121(12), 5–30. <https://doi.org/10.1002/2016JD025506>.Received
- World Meteorological Organization. (2008). *Guide to Meteorological Instruments and Methods*

of Observation. *WMO-No.8 (CIMO Guide)*, Geneva CH., 5.

Zhang, F., Zhang, H., Hagen, S. C., Ye, M., Wang, D., Gui, D., Zeng, C., Tian, L., & Liu, J. (2015). Snow cover and runoff modelling in a high mountain catchment with scarce data: effects of temperature and precipitation parameters. *Hydrological Processes*, 29(1), 52–65. <https://doi.org/10.1002/hyp.10125>

### CHAPTER 3. IMPLICATIONS AND FUTURE WORK

This research characterized temperature-elevation gradient (TEG) and dew point temperature elevation gradient (DTEG) for a small snow-dominated watershed within the Cache la Poudre Basin. It also investigated how TEG and DTEG affect snowmelt modeling by using observed and published values. We found that generally the ELR is close to the daytime TEG but nighttime values are often positive and dissimilar to published values. This difference produced a modeled snow-all-gone difference of up to 6 days. The average hourly DTEG value was  $-1.26^{\circ}\text{C}$  colder than the Kunkel (1989) DTEG. This difference between observed DTEG and the Liston and Elder  $T_d$  provided minimal differences in snowmelt when manipulating the incoming longwave radiation within the net radiation variable in the temperature and radiation index snowmelt model. Melt factors for the temperature index model can be applied to other sites with similar regimes based on this study (e.g., Lake Irene SNOTEL and Joe Wright Creek SNOTEL). Conversely, melt factors for the temperature and radiation index model did not perform as well when applying melt factors developed from a different elevation (Joe Wright SNOTEL) in the latter portion of the melt season as net shortwave radiation increase. For example, on June 10, 2021, model scenario A (base case) is 29.5 percent different than observed SWE and earlier in the season there were differences as low as 0.1 percent.

Extensive research is ongoing within the Cache la Poudre basin to study the impacts of wildfire on hydrology, geomorphology, and ecology. Wildfires often cause more pronounced spatial variability in hydrometeorological variables (Harpold et al., 2014). With this study, we have a better understanding of TEG and DTEG at high-elevation areas within this basin, yet

future work can add to this. Such future work includes modeling snowmelt across all elevations of the Joe Wright Creek watershed, and translating snowmelt to streamflow. This will ultimately indicate how TEG and DTEG affect streamflow characteristics, such as, peak streamflow magnitude and timing. Additionally, mapping possible cold air drainage locations (Lundquist et al., 2008) could enhance our understanding of the distribution of temperature. Moreover, adding additional sensors, particularly anemometers and radiometers, in the alpine or at higher elevations beyond just at Joe Wright SNOTEL would help refine snowmelt modeling and possibly provide data to assess wind thresholds to estimate TEG or DTEG. For example, if it is windy, then cold air drainage does not occur.

As the climate continues to warm and meteorological extremes are realized, it is important to understand how this may affect water resources. Future evaluations could examine how TEG and DTEG would impact snowmelt under future climate change scenarios. In our study, the alpine provided variable results and in some of the DTEG analyses, the alpine BM sensors were removed to yield an improved correlation. Further research needs to examine processes that occur in the alpine and how climate change will impact those processes.

### **3.1 References**

- Harpold, A. A., Biederman, J. A., Condon, K., Merino, M., Korgaonkar, Y., Nan, T., Sloat, L. L., Ross, M., & Brooks, P. D. (2014). Changes in snow accumulation and ablation following the Las Conchas Forest Fire, New Mexico, USA. *Ecohydrology*, 7, 440–452. <https://doi.org/10.1002/eco.1363>
- Lundquist, J. D., Pepin, N., & Rochford, C. (2008). Automated algorithm for mapping regions of cold-air pooling in complex terrain. *Journal of Geophysical Research Atmospheres*, 113(22). <https://doi.org/10.1029/2008JD009879>
- Kunkel, K. E. (1989). Simple Procedures for Extrapolation of Humidity Variables in the Mountainous Western United States. *Journal of Climate*, 2, 656–669.

## APPENDIX A: SITE MAPS AND FIELD DATA LOCATIONS

Appendix A includes site maps of Joe Wright Creek (JWC) and locations of sensors and SWE measurements. The site maps include land cover (Figure A-1), aspect (Figure A-2), and slope (Figure A-3). Table A-1 includes sensor names, elevation, and installation date. Table A-2 includes SWE measurements and collection dates for the 2021 melt season.

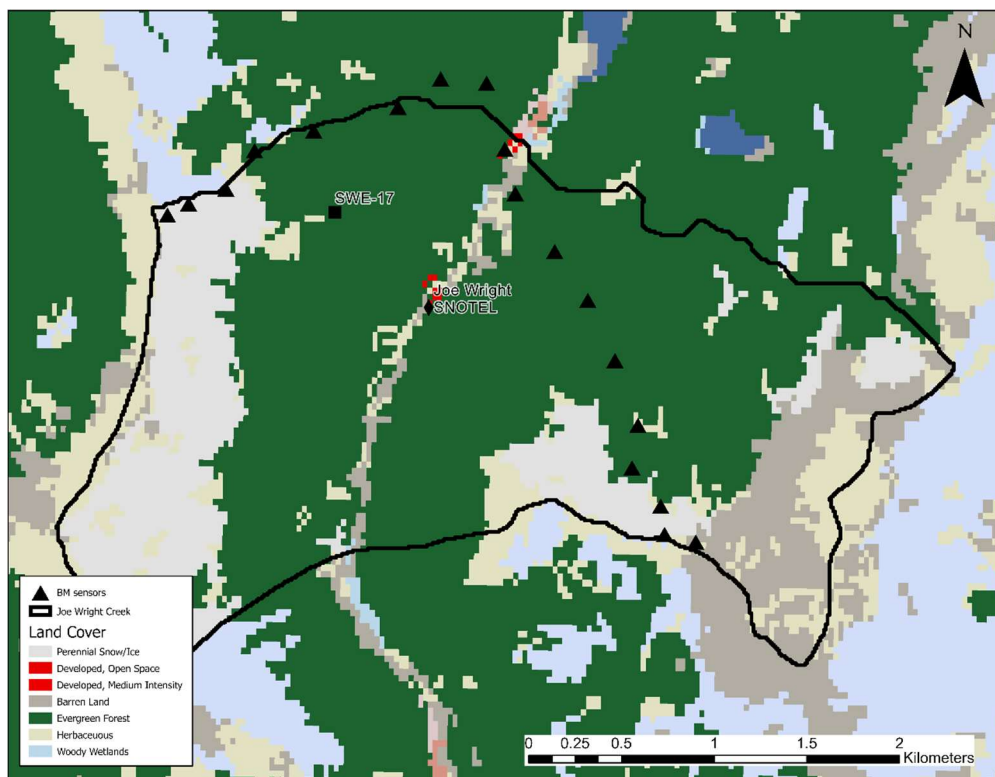


Figure A-1. Land cover of JWC.

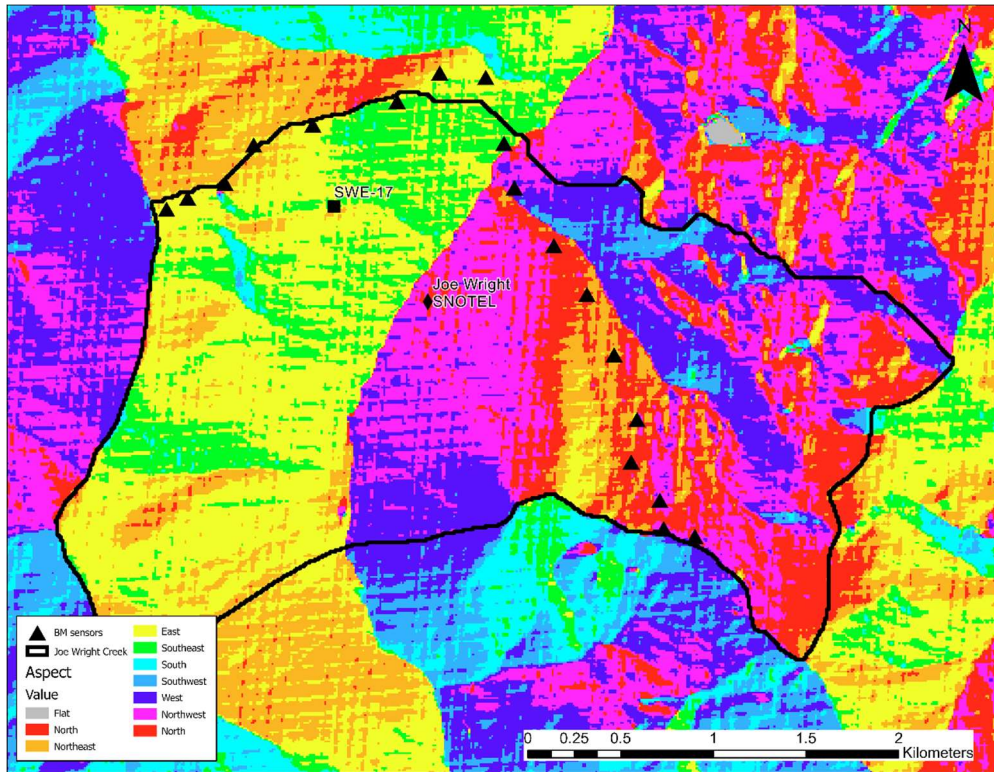


Figure A-2. Aspect of JWC.

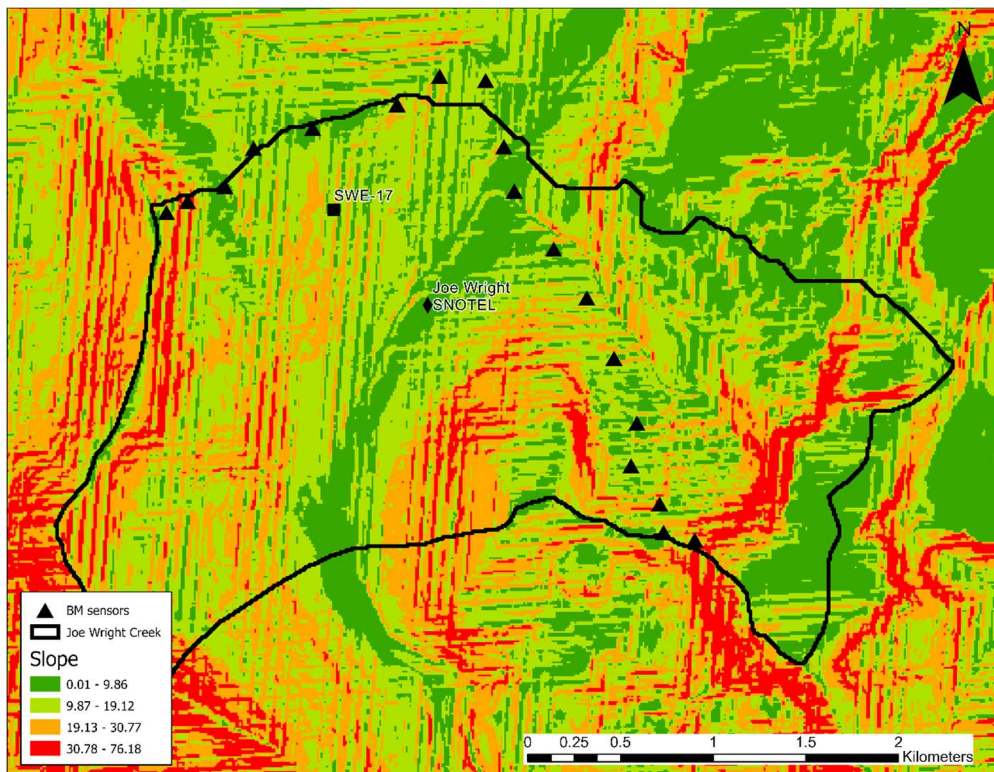


Figure A-3. Slope of JWC.

Table A-1. Temperature and relative humidity sensor elevation and installation date.

ID	Elevation (m)	Date installed
HD1	3059	April 19, 2020
HD2	3104	April 19, 2020
HD3	3158	May 1, 2020
HD4	3216	May 1, 2020
HD5	3268	May 1, 2020
HD6	3312	May 1, 2020
HD7	3370	May 1, 2020
HD8	3410	April 10, 2021
HD9	3450	April 10, 2021
MP1	3051	April 19, 2020
MP2	3092	April 19, 2020
MP3	3144	April 19, 2020
MP4	3197	April 19, 2020
MP5	3248	April 19, 2020
MP6	3303	April 19, 2020
MP7	3358	April 19, 2020
MP8	3407	April 10, 2021
MP9	3453	April 10, 2021

Table A-2. Date of SWE samples collected in JWC during the 2021 melt season.

ID	1-May	12-May	27-May	10-Jun
SWE-1	x			
SWE-2	x			
SWE-3	x			
SWE-4	x		x	
SWE-5	x		x	
SWE-6	x			
SWE-7	x			
SWE-8	x	x	x	x
SWE-9	x	x	x	x
SWE-10	x	x	x	x
SWE-11	x	x	x	x
SWE-12	x	x	x	x
SWE-13	x	x	x	x
SWE-14	x	x	x	x
SWE-15	x	x		x
SWE-16	x	x	x	x
SWE-17	x	x	x	x
SWE-18	x			x
SWE-19	x			x
SWE-20		x	x	x
SWE-21			x	x
SWE-22		x	x	x
SWE-23		x	x	x
SWE-24	x			
SWE-25	x			
SWE-26	x			
SWE-27	x			
SWE-28	x			
SWE-29	x			
SWE-30	x			
SWE-31	x			
SWE-32	x		x	
SWE-33	x		x	
SWE-34	x		x	
SWE-35	x		x	
SWE-36	x		x	
SWE-37	x		x	
SWE-38	x		x	
SWE-39	x		x	
SWE-40	x		x	

## APPENDIX B: RESULTS

Appendix B includes graph of air temperature-elevation gradients (TEG) and dew point temperature-elevation gradients (DTEG) for April 2020 through June 2021 (Figures B-1 through B-4). Figure B-5 is air temperature versus dew point temperature for May and June 2020 and 2021. Figures B-6 and B-7 are TEG and DTEG values compared to wind direction. Figure B-8 presents observed snowmelt at the Joe Wright SNOTEL versus modeled. Figure B-9 shows the temperature melt factors used in the temperature index snowmelt model.

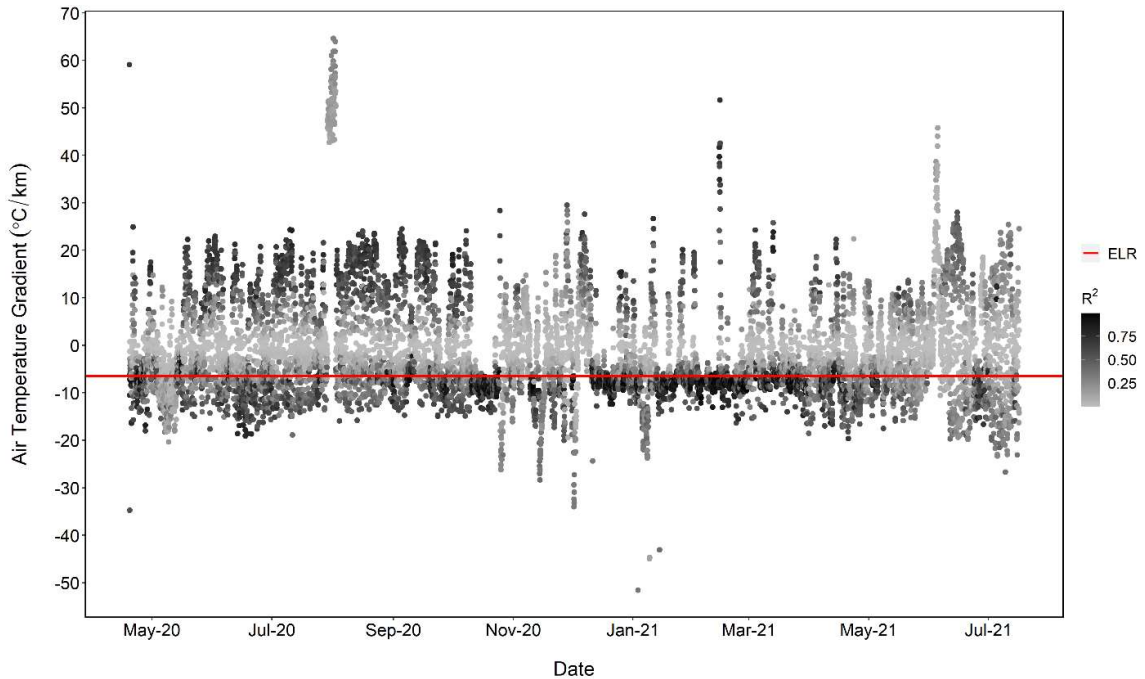


Figure B-1. TEG for April 2020 to July 2021. The red line represents the ELR. The shading of the points represents the  $R^2$  value.

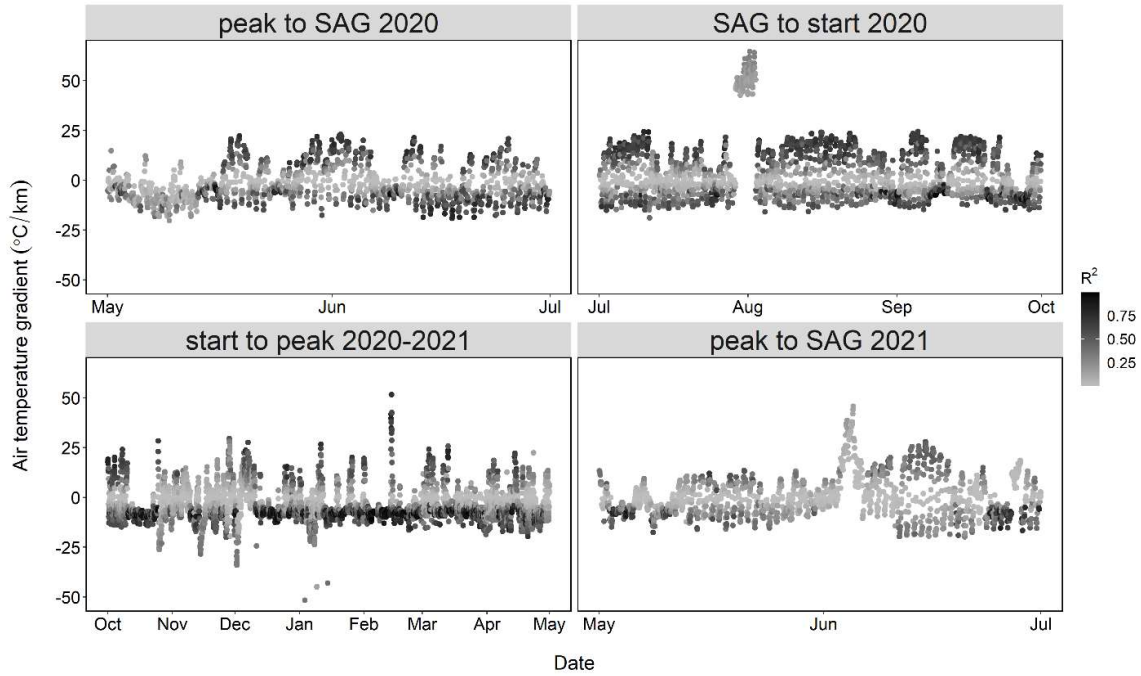


Figure B-2. TEG for 2020 and 2021 season. The shading of the points represents the R<sup>2</sup> value.

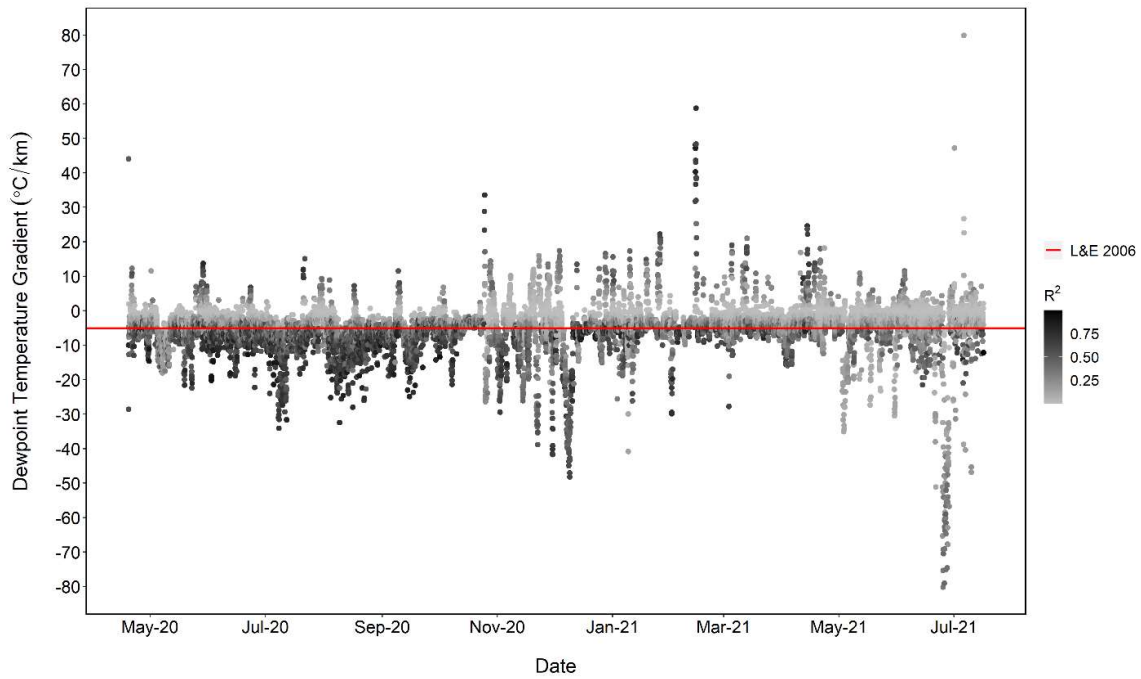


Figure B-3. DTEG for April 2020 to July 2021. The red line represents the Kunkel (1989) DTEG. The shading of the points represents the R<sup>2</sup> value.

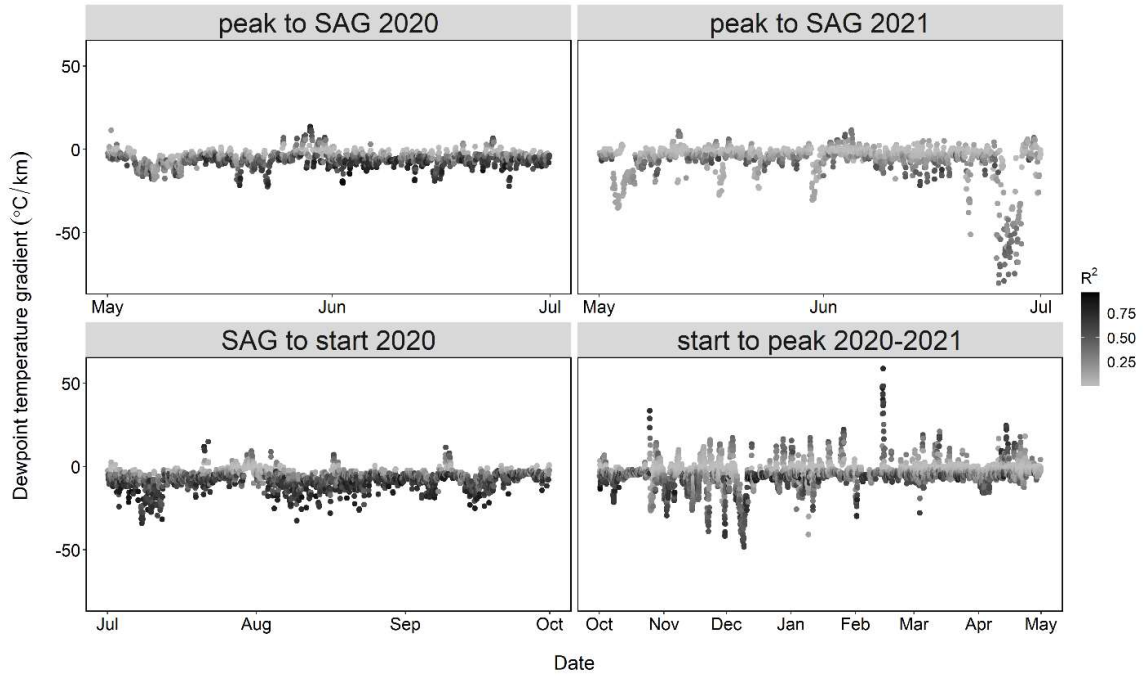


Figure B-4. DTEG for season 2020 and 2021. The shading of the points represents the R<sup>2</sup> value.

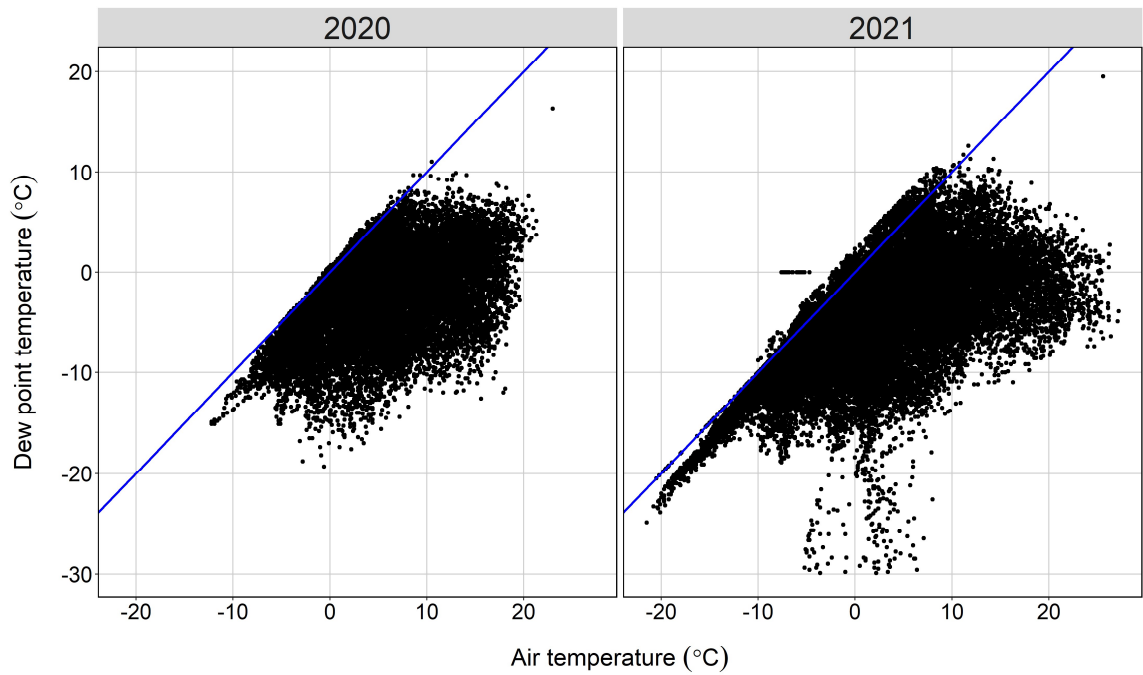


Figure B-5. Air temperature versus dew point temperature for May and June 2020 and 2021. The blue line represents a 1:1 line.

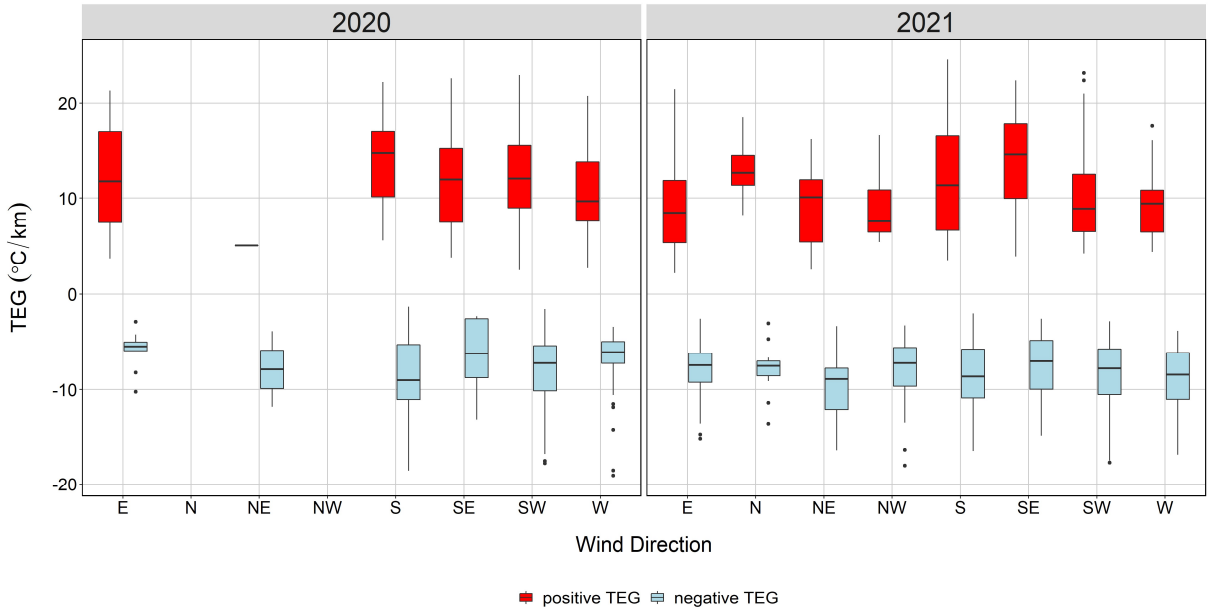


Figure B-6. TEG and wind direction for May and June 2020 and 2021.

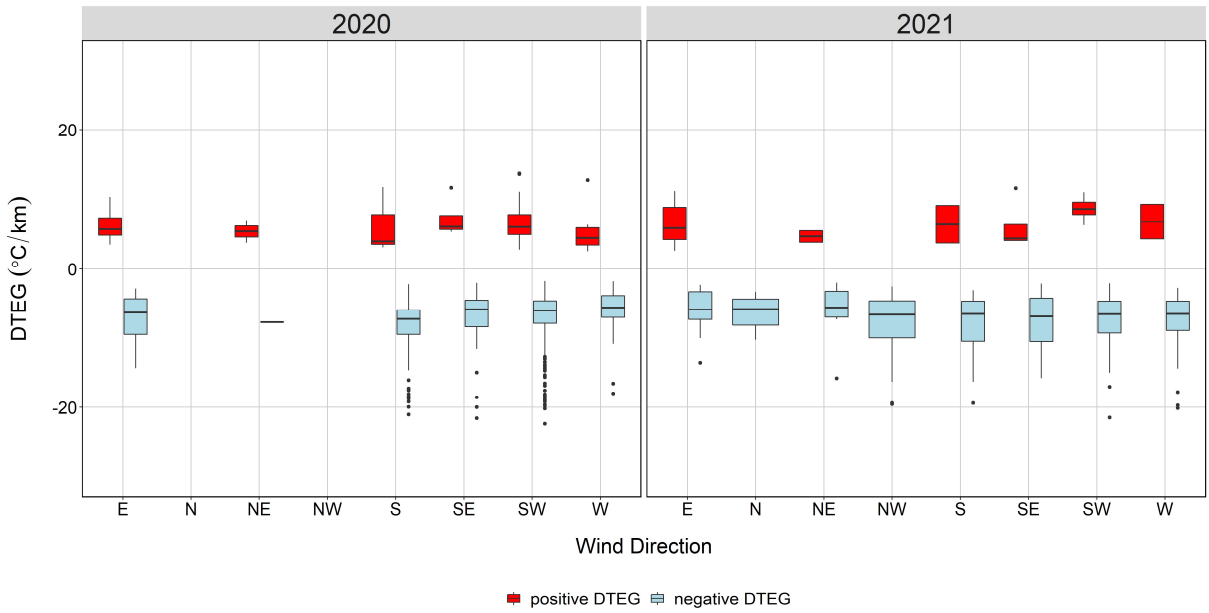


Figure B-7. DTEG and wind direction for May and June 2020 and 2021.

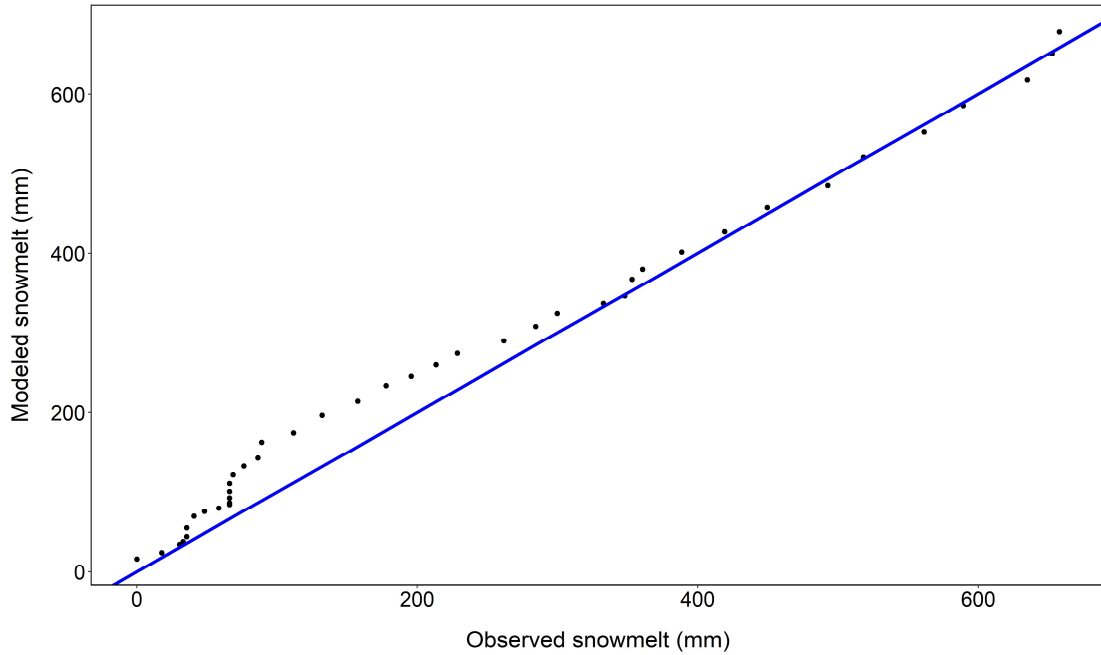


Figure B-8. Observed snowmelt versus modeled snowmelt for May and June 2021 at the Joe Wright SNOTEL. The modeled snowmelt uses the temperature and radiation index snowmelt model melt factors and reference temperature. The blue line represents a 1:1 line. The NSE between modeled and observed is 0.97.

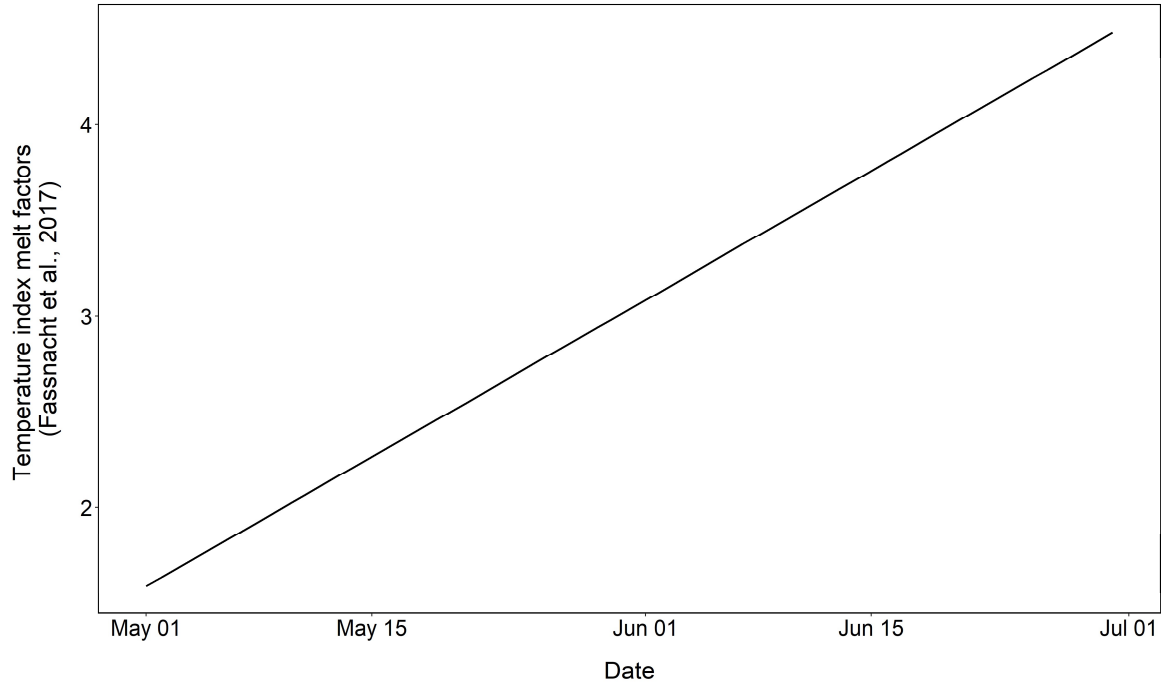


Figure B-9. Continuous temperature melt factors incorporated in the temperature index snowmelt models (obs T & simpler model and local lapse T & simpler model) developed from the Lake Irene SNOTEL station (Fassnacht et al., 2017).